Revision 1

Word Count: 12,227

Crystal habit (tracht) of groundmass pyroxene crystals recorded magma ascent paths during the 2011 Shinmoedake eruption

Shota H. Okumura[1*], Mayumi Mujin[2], Akira Tsuchiyama[3,4,5], and Akira Miyake[1]

Affiliations:

[1]Department of Geology and Mineralogy, Graduate School of Science, Kyoto University, Kitashirakawaoiwake-cho, Sakyo-ku, Kyoto 606-8502, Japan

[2]Department of Earth Science, Graduate School of Science, Tohoku University, 6-3, Aramaki-Aza-Aoba, Aobaku, Sendai 980-8578, Japan

[3]Research Organization of Science and Technology, Ritsumeikan University, 1-1-1 Nojihigashi, Kusatsu, Shiga 525-8577, Japan

[4]CAS Key Laboratory of Mineralogy and Metallogeny/Guangdong Provincial Key Laboratory of Mineral Physics and Materials, Guangzhou Institute of Geochemistry, Chinese Academy of Sciences, 511 Kehua Street, Wushan, Tianhe District, Guangzhou 510640, China

[5]CAS Center for Excellence in Deep Earth Science, Guangzhou 510640, China

*Corresponding author: S.H. Okumura, okumura@kueps.kyoto-u.ac.jp

Abstract

The morphologies and size distributions of groundmass crystals record conditions of magma ascent through volcanic conduits. Nevertheless, morphological information (such as crystal shapes) has not been incorporated into crystal size distributions (CSDs). Here, we focused on the crystal habit, especially the shape variation due to the combination of (*hk*0) faces (hereafter "tracht") of pyroxene microlites and nano-crystals, and measured CSDs for each crystal habit (tracht) to more comprehensively characterize the crystallization kinetics. We refer to the CSDs measured for each tracht as "tracht-specific CSDs." Pyroclasts from the 2011 eruption of Shinmoedake (Kirishima volcano group, Japan) were observed by field-emission scanning electron microscopy, electron backscatter diffraction analysis, synchrotron radiation X-ray computed nanotomography, and transmission electron microscopy. The samples contain groundmass pyroxenes of two main trachts: octagonal prisms consisting of {100}, {010}, and {110} faces and hexagonal prism lacking {100} faces. The pumice clasts formed by different eruption styles showed different trends of tracht-specific CSDs. Sub-Plinian pumice clasts were characterized by octagonal microlites (1–10 μm wide) and numerous hexagonal nano-crystals (0.2–2 μm wide), and a Vulcanian pumice clast with the same glass composition showed the same characteristics. In contrast, Vulcanian pumice clasts with more evolved glass compositions contained mostly octagonal pyroxenes. The tracht-specific CSDs and growth zonations indicate a change from octagon-dominant to hexagon-dominant growth conditions during syneruptive ascent. We infer that the hexagonal tracht resulted from a large degree of effective undercooling due to rapid decompression in the shallow conduit. Moreover, the texture of the less-evolved Vulcanian pumice indicates that a portion of the magma erupted on the Vulcanian eruption followed almost the same ascent paths just prior to the fragmentation as those during the sub-Plinian eruptions, and thus the Vulcanian eruption may have involved the rapid ascent of deeper magma. We propose that tracht analyses of groundmass pyroxenes provide detailed information about time-evolution of magma conditions during syneruptive ascent.

Keywords: pyroxene, crystal habit, crystal size distribution, nanolite, magma ascent

Introduction

Degassing mechanisms within volcanic conduits involve interrelated magmatic properties and processes, and affect both the eruptive style and evolution of volcanoes (Cassidy et al. 2018). One of the most important parameters affecting the various magmatic feedbacks is magma ascent rate. The evolution of ascent rate in conduits is related to syneruptive processes such as volatile exsolution, crystallization, and rheological evolution of magmas (e.g., Gonnermann and Manga 2007; Cassidy et al. 2018; La Spina et al. 2016, 2021) and thus is important for elucidating the depths where transitions in eruptive style originate and the mechanisms of those transitions. Magma ascent paths are preserved in the properties of groundmass crystals, such as their number densities and morphologies (e.g., equant, tabular, acicular, euhedral, swallowtail, dendritic).

Groundmass crystallization kinetics (i.e., nucleation and growth) have been investigated both experimentally and in natural samples (e.g., Cashman 1992; Hammer and Rutherford 2002; Couch et al. 2003; Brugger and Hammer 2010a). Recent studies have focused on constraining nucleation and growth rates (Shea and Hammer 2013; Arzilli et al. 2015, 2016a; Giuliani et al. 2020), nucleation events through time (Arzilli and Carroll

2013; Polacci et al. 2018; Le Gall et al. 2021; Arzilli et al. 2022), nucleation delay (Arzilli et al. 2020; First et al. 2020; Rusiecka et al. 2020; Rusiecka and Martel 2022), and crystal growth in real time (Polacci et al. 2018; Arzilli et al. 2019, 2022; Le Gall et al. 2021). These contributions have deepened understanding of the crystallization kinetics under disequilibrium conditions.

The kinetics of disequilibrium crystallization results in the various crystal textures. Crystal habits are controlled by the degree of effective undercooling (ΔT_{eff}) imposed from cooling and decompression-induced dehydration, and are thus important clues to investigate magma ascent and/or solidification histories via the extent of ΔT_{eff} (e.g., Lofgren 1974, 1980; Donaldson 1976; Hammer and Rutherford 2002; Couch et al. 2003; Castro and Dingwell 2009; Shea and Hammer 2013; Waters et al. 2015; Giuliani et al. 2020; Arzilli et al. 2022). Moreover, the crystal habits have a strong influence on magma rheology and dynamics (e.g., Mueller et al. 2010; Mader et al. 2013; Le Gall et al. 2021; Arzilli et al. 2022). On the other hand, crystal number densities are also used to estimate ascent conditions, such as crystal size distributions (CSDs; Marsh 1998) and the water exsolution rate meter (Toramaru et al. 2008). In particular, the slopes of CSDs obtained from pyroclasts reflect temporal changes in the balance between nucleation and growth during magmatic processes (e.g., Cashman and Marsh 1988; Marsh 1998; Armienti 2008; Mujin et al. 2017; Okumura et al. 2022a).

In this study, we introduce a concept of "tracht." In contrast to the term "crystal habit," "tracht" is a German term referring to the variation of crystal shapes due to the combination and degree of development of faces (Sunagawa 2005). Although "crystal habit" refers to the shape differences including "tracht," this English term is generally used to specify shapes in a broader sense (cf. Franke 1989; Fig. 2.15a in Schupsky 2020). For instance, a hexagonal prism is distinguished from an octagonal prism under the concept of "tracht," whereas the concept of "crystal habit" generally does not distinguish between these shapes and treats them as a prismatic and/or euhedral shape. Since the former concept (i.e., tracht) is not defined in English (Sunagawa 2005; Schupsky 2020), we hereafter use the term "tracht" in this study.

In single-step decompression experiments on hydrous dacite magma, Okumura et al. (2022b) showed that the tracht of groundmass pyroxenes changes from octagonal to hexagonal as ΔT_{eff} increases. Since these trachts are easily classified under 2D observation, CSDs can be measured for each shape. In this study, we report the CSDs of groundmass pyroxenes measured for each tracht (i.e., octagonal, heptagonal, and hexagonal; hereafter "tracht-specific CSDs"). Although there are many literatures that have focused on crystal shapes, such as crystal habits and interface-controlled versus diffusion-controlled growth textures (e.g., Lofgren 1974; Donaldson 1976; Lofgren 1980; Hammer and Rutherford 2002; Shea and Hammer 2013; Giuliani et al. 2020; Arzilli et al. 2022), this study differs from the previous attempts in that it involves plane indices as crystallographic properties. The tracht-specific CSDs will push past the limits of the conventional CSD analyses by relating the growth texture to the temporal evolution of nucleation during syneruptive magma ascent, as described below.

The rates of crystal nucleation and growth generally escalate as the extents of decompression and resultant ΔT_{eff} increase; the former tends to show a greater escalation than the latter (e.g., Hammer and Rutherford 2002; Couch et al. 2003; Brugger and Hammer 2010a; Mollard et al. 2012; Shea and Hammer 2013; Arzilli et al. 2016a; Mollo and Hammer 2017). In a closed magmatic system with variable rates of nucleation and growth, CSD slopes are considered to reflect the significant increase in nucleation rate during magma ascent (Marsh 1998). On the other hand, the large variations in syneruptive crystal growth rates (e.g., Couch et al. 2003; Brugger and Hammer 2010b; Befus and Andrews 2018) also can affect the resultant CSD and render its interpretation difficult. For example, Okumura et al. (2022a) showed that slow crystallization (both nucleation and growth) can result in a CSD slope similar to that of rapid crystallization by using the formulas of Marsh (1998). As a measure against this, a new expression of CSDs proposed by Okumura et al. (2022a) reduces the effects of variable growth rates by adopting 3D short-axis length instead of 3D long-axis length as crystal size. This is because rock-forming minerals tend to elongate with increasing ΔT_{eff} (e.g., Kouchi et al. 1983; Hammer and Rutherford 2002; Shea and Hammer 2013; Arzilli et al. 2022), and thus the growth rates along the long- and short-axes are probably the most and least susceptible to ΔT_{eff}, respectively. The slopes of the CSDs plotted against 3D short-axis length are controlled more strongly by nucleation rate, enabling us to investigate temporal changes in nucleation rate more reliably (Okumura et al. 2022a).

In contrast, it is still difficult to determine changes of growth rate during syneruptive ascent from the CSDs of pyroclasts, because magmas experience a wide range of ΔT_{eff} and thus the significant changes in nucleation rate during the ascent, as indicated by continuous decompression experiments (e.g., Brugger and Hammer 2010a; Mollard et al. 2012; Befus and Andrews 2018). In such a situation, it is not possible to circumvent the overwhelming effect of the variable nucleation rate on the CSD slopes (cf. Marsh 1998), which in turn prevents the extraction of the variation in growth rate from the slopes unless parameterization analyses (Armienti 2008) are performed successfully. Since the crystal textures including CSDs and crystal habits (and probably trachts) are controlled by the interplay between nucleation and growth depending on ΔT_{eff} (e.g., Hammer and Rutherford 2002; Couch et al. 2003; Hammer 2008; Mollard et al. 2012; Shea and Hammer 2013; Mollo and Hammer 2017; Mangler et al. 2022), the temporal change of nucleation should be examined in relation to growth so as to decipher syneruptive crystallization kinetics.

Although the conventional CSD analyses are not suitable to investigate the temporal change of nucleation in synchronization with that of growth as mentioned above, this investigation can be possible if growth textures are incorporated into CSDs as the indicator of growth conditions such as growth rate and ΔT_{eff}. In this context, the tracht-specific CSDs are expected to provide a comprehensive view of crystallization kinetics and reveal more details about temporal changes of ΔT_{eff} and magma ascent dynamics.

To investigate whether the tracht-specific CSDs record syneruptive magma paths, we analyzed groundmass pyroxene crystals in pyroclasts from the 2011 eruption of Shinmoedake (Kirishima volcano group, Japan). The 2011 eruption of Shinmoedake included sub-Plinian eruptions and subsequent Vulcanian eruptions. The different magma ascent conditions in the shallow conduit during eruptions of these two styles have been investigated using groundmass plagioclase CSDs measured from scanning electron microscope (SEM) images (Mujin and Nakamura 2014; Mujin et al. 2017; Suzuki et al. 2018). In addition, Okumura et al. (2022a) directly acquired 3D CSDs of groundmass pyroxenes by X-ray computed tomography and demonstrated that nucleation kinetics of pyroxenes also differed between the two styles. Therefore, the tracht-specific CSDs of groundmass pyroxenes in pumices from sub-Plinian and Vulcanian eruptions of the 2011 Shinmoedake eruption should exhibit different trends.

In addition to their tracht-specific CSDs, the internal textures of groundmass pyroxene crystals record magmatic conditions as compositional zoning (e.g., Ubide and

Kamber 2018; Masotta et al. 2020). Therefore, we observed the textures within individual crystals to corroborate the magma ascent paths inferred from the CSDs. Based on the inferred crystallization kinetics of groundmass pyroxenes, we aim to better understand the conduit processes during the 2011 Shinmoedake eruption.

Sample description

Shinmoedake is an andesitic volcano in the Kirishima volcano group, southern Kyushu, Japan. The chronology of the 2011 Shinmoedake eruption has been well documented (e.g., Kozono et al. 2013; Nakada et al. 2013; Kato and Yamasato 2013). The main phase of the eruptive activity (26–31 January 2011) was characterized by three sub-Plinian eruptions and the subsequent extrusion of a lava dome within the crater, associated with intermittent Vulcanian eruptions. This activity was followed by repeated Vulcanian eruptions and explosive events from 1 February to 13 March 2011. Here, we examined seven pyroclasts: three gray pumice clasts from the sub-Plinian eruptions and three gray pumice clasts and one dense juvenile fragment from the Vulcanian eruptions. These samples were collected on 24 July 2011 at Takachihogawara, 3 km south of

Shinmoedake crater; collection details are reported in Mujin and Nakamura (2014). Although the precise eruptions that produced the Vulcanian samples have not been determined, they most likely occurred on 1 or 11 February or 13 March (Mujin et al. 2017). Nonetheless, we were able to easily distinguish the Vulcanian pumices from the sub-Plinian pumices because the former were larger than the latter.

The seven samples are classified into two groups according to the chemical compositions of their groundmass glasses (Mujin and Nakamura 2020): those of the three sub-Plinian pumice clasts (sP_a, sP_b, and sP_c), one Vulcanian pumice clast (V-L), and the dense juvenile fragment (V-L-djf) contained <71 wt% SiO_2 (low-SiO_2 samples), whereas those of the other two Vulcanian pumice clasts (V-H_a and V-H_b) contained >71 wt% SiO_2 (high-SiO_2 samples). Two of the pumice clasts (sP_a and V-H_a) and the dense juvenile fragment (V-L-djf) were previously analyzed by Okumura et al. (2022a) and Mujin et al. (2017), respectively. The dense fragment (V-L-djf) probably originated from the welding of sub-Plinian pumice at the crater, because its glass composition is similar to that of the sub-Plinian pumice (Table 1) and its degassed dense texture with nano-crystals smaller than 30 nm in diameter indicates suppressed crystal growth at high ΔT_{eff} in the dehydrated melt with low diffusivity (Mujin et al., 2017; Mujin and Nakamura 2020). The average compositions of each sample are reported in Table 1.

The samples contain phenocrysts (>100 μm) of plagioclase, clinopyroxene (Cpx), orthopyroxene (Opx), olivine, magnetite, and ilmenite, some showing reaction rims due to mixing with a higher temperature magma (Suzuki et al. 2013; Tomiya et al. 2013). Their groundmasses are charged with crystals of plagioclase, pyroxenes, and Fe-Ti oxides (ca. 0.1–10 μm wide); those thinner than 1 μm are referred to as nanolites, and those larger as microlites. Because most groundmass pyroxene crystals show parallel intergrowths of Opx and Cpx (Mujin et al. 2017), we treated them as a single pyroxene phase, except when analyzing internal textures.

Analytical procedures

The textures of groundmass pyroxenes in the pumices were analyzed with a field-emission SEM (FE-SEM). The chemical compositions of groundmass glasses in all samples were measured with a coupled energy-dispersive X-ray spectrometer (EDS). To obtain 3D aspect ratios (*S*:*I*:*L*, where *S*, *I*, and *L* are the short, intermediate, and long axes) of pyroxene crystals, which are necessary to stereologically correct the CSDs, we conducted synchrotron radiation X-ray computed nanotomography (SR-XnCT). The SR-XnCT specimens were prepared with a focused ion beam (FIB) system, and the average 3D aspect ratios of groundmass pyroxenes were acquired for each pumice sample. Using these values, we calculated tracht-specific CSDs of groundmass pyroxenes in each sample. We did not calculate the CSD of the dense fragment V-L-djf because we focused on the pumice samples to investigate syneruptive ascent conditions rather than post-eruptive processes.

We determined the crystallographic indices of the faces of groundmass pyroxenes by combining electron backscatter diffraction (EBSD) analysis and SR-XnCT. The EBSD analysis was performed on a relatively large pyroxene microlite (~7 μm wide) with a hexagonal cross section in V-L-djf to determine its crystallographic orientation. The crystal was then prepared as a SR-XnCT specimen with the FIB system and observed to obtain its 3D outline. By combining these data, we acquired the face indices of the hexagonal crystal.

Moreover, we observed groundmass pyroxene crystals in three pumice samples (sP_a, V-H_a, and V-L) using a transmission electron microscope (TEM). Ultrathin sections were prepared from the samples using FIB systems. In addition to determination of mineral phases and crystallographic orientations by selected-area electron diffraction (SAED) patterns, we investigated compositional zoning in crystals by EDS analyses in scanning TEM (STEM) mode. An overview of the analytical procedures used is shown in Figure S1 in Online Resource 1.

FE-SEM-EDS

Quantitative compositional analyses of groundmass glasses were performed using a JEOL JSM-7001F FE-SEM coupled with an Oxford Instruments X-Max150 EDS detector and its associated analytical software *Aztec* at Kyoto University. We analyzed 50 square regions (~1 × 1 μm) in each sample for 40 s each at a working distance of 10 mm, an acceleration voltage of 15 kV, and a beam current of ~0.3 nA. We corrected for losses of Na and K during the measurements by calibration against analyses of larger rectangular regions (>400 μm^2).

For textural analyses, backscattered electron (BSE) images of polished sections of the pumice samples were obtained at an acceleration voltage of 15 kV and a working distance of 10 mm using the FE-SEM. Each BSE image was a rectangular area of 127 × 95 μm^2 with an image resolution of ca. 25 nm/pixel. To identify their trachts, magnified images of the pyroxene crystals in the analyzed areas were obtained at an acceleration voltage of 10 kV.

EBSD

EBSD analysis of the large hexagonal microlite in V-L-djf was performed using a SEM equipped with a tungsten filament (FEI Quanta 200 3DS) and a HKL EBSD system with *Channel 5* software (Oxford Instruments) at Kyoto University. Using an acceleration voltage of 15 kV, a working distance of 20 mm, and the lattice parameters of diopside (a = 9.75 Å, b = 8.99 Å, c = 5.25 Å, β = 105.6°), the crystallographic orientation of the microlite was determined before SR-XnCT observation.

FIB systems

For SR-XnCT observations, we extracted one or two equant specimens about 20–25 μm wide from each sample (Table 2) using a FEI Quanta 200 3DS FIB system at Kyoto

University. The extracted regions were distinct from the areas of FE-SEM textural analyses. Each specimen was then mounted on a tungsten needle. A Ga^+ ion gun was used at an acceleration voltage of 30 kV and a beam current of 0.030–65 nA. Details of the specimen preparation for SR-XnCT are reported in Miyake et al. (2014).

For TEM observation, ultrathin sections about 100 nm thick were prepared using FIB systems (FEI Quanta 200 3DS and FEI Helios NanoLab G3 CX) at Kyoto University. The Ga^+ ion guns were used at 30 kV and 0.083–65 nA for thinning, and at 5 kV and 16 pA for final processing.

SR-XnCT

We acquired the 3D shapes of groundmass pyroxene crystals by SR-XnCT at beamline BL47XU of the Spring-8 synchrotron facility in Hyogo, Japan (Uesugi et al. 2006; Takeuchi et al. 2009). The SR-XnCT measurements were performed in absorption-contrast mode (e.g., Cloetens et al. 1997; Mancini et al. 1998; Tsuchiyama et al. 2013; Arzilli et al. 2016b) using an X-ray imaging system with a Fresnel zone plate at a single X-ray energy of 7.35 keV, providing isotropic voxel (volumetric pixel) sizes of 25–

78 nm on a side (Table 2) for an effective specific resolution of ~200 nm. Projection images were acquired every 0.1° during a total sample rotation of 180°, resulting in 1,800 projections per specimen. The 3D CT images were reconstructed from the projection images using a convolution back-projection algorithm (Nakano et al. 2000). Details of the CT imaging procedures are reported in Matsumoto et al. (2019).

Except for four CT specimens (sP_a-1, sP_a-2, and V-H_a-1 from Okumura et al. 2022a, and V-L-djf), the CT images were denoised using iterative nonlocal means (Bruns et al. 2017) before binarization: this process reduced the effort involved in binarization by smoothing the insides of crystals without affecting the quality of the extracted 3D data. Pyroxenes were distinguishable from the other minerals on the basis of pixel values; therefore, we binarized the images with thresholds based on visual inspection, removed blurring of the binary images by erosion and dilation by 1 voxel, and extracted the 3D pyroxene crystal data using the software package *Slice* (Nakano et al. 2006). We determined the triaxial lengths *S*, *I*, and *L* by ellipsoid fitting in *Slice* (e.g., Tsuchiyama et al. 2011). These measurements were restricted to crystals that were entirely contained within the specimens, larger than 5 voxels wide, and readily separated from other crystals. The average 3D aspect ratio of groundmass pyroxenes in each pumice sample was calculated to obtain the necessary information for determining CSDs from the BSE images (Table 2).

Although we analyzed six pumice samples to obtain the average 3D aspect ratios in this study, two of the pumice samples (i.e., sP_a and V-H_a) were already observed by SR-XnCT by Okumura et al. (2022a) (our CT specimens sP_a-1, sP_a-2, V-H_a-1, and V-H_a-2 correspond to their specimens sP_1, sP_2, Vul_1, and Vul_2, respectively). They reported 3D CSDs of groundmass pyroxenes for the samples sP_a and V-H_a, whereas we did not obtain 3D CSDs from the other samples. Tracht-specific CSDs could not be obtained directly from the CT data because the spatial resolution was insufficient to recognize nanolite trachts. Thus, tracht-specific CSDs were obtained from the SEM images using the 3D aspect ratios (see *Acquisition of tracht-specific CSDs*).

TEM

Ultrathin sections prepared from three pumice samples (sP_a, V-H_a, and V-L) were observed under a JEOL JEM-2100F TEM equipped with a Gatan Orius 200D CCD camera and a JEOL JET-2300T EDS detector at an acceleration voltage of 200 kV. To determine mineral phases and crystallographic orientations, SAED patterns were analyzed using *DigitalMicrograph* (Gatan) and *ReciPro* (Seto and Ohtsuka 2022) software. For quantitative X-ray analyses by STEM, we used the ζ-factor method (Watanabe and Williams 2006). To achieve the accurate electron beam current measurements required for the ζ-factor method, appropriate calibration was performed with the CCD camera beforehand. Furthermore, we acquired annular dark-field STEM (ADF-STEM) images of pyroxene crystals perpendicular to their *c*-axes to observe their compositional zoning at higher resolution.

Acquisition of tracht-specific CSDs

The FE-SEM BSE images of pumice groundmasses were analyzed using *ImageJ* software to measure the examined groundmass area (i.e., groundmass crystals + glass, excluding vesicles) and the widths of the best fit ellipses to the cross sections of pyroxene crystals. The analyzed samples contained groundmass pyroxene crystals with octagonal, heptagonal, and hexagonal trachts (Fig. 1a); therefore, each pyroxene cross section was classified into one of these tracht groups based on BSE images at higher magnification.

Crystals were classified based on the number of faces between a pair of parallel faces (Okumura et al. 2022b). For example, the octagonal and hexagonal trachts have three and two faces, respectively, between each pair of parallel faces, whereas the heptagonal tracht has the properties of the octagonal tracht on one side of a pair of parallel faces and those of the hexagonal tracht on the other side (Fig. 1a). Crystals that were difficult to classify as belonging to a particular tracht were classified as “other”. If cross sections were incomplete (e.g., those at crystal edges or corners), we classified them based on the remaining faces if a pair of parallel faces was present for reference; otherwise, those showing no pairs of parallel faces in the plane of the BSE image were classified as “other” (Fig. 1b). When multiple crystals were attached to each other, each segment was classified in the same way (Fig. 1c). The analyzed areas and the number of crystals observed in each tracht are shown in Table 3.

Then, the datasets of all analyzed crystals and each tracht group were converted to a conventional CSD (i.e., including all crystal trachts) and tracht-specific CSDs, respectively, using *CSDCorrections* ver. 1.6 (Higgins 2000). *CSDCorrections* converts cross-sectional widths into 3D long-axis lengths (L) using the 3D aspect ratio S:I:L. We used the average 3D aspect ratio determined by SR-XnCT for each sample, regardless of tracht. Although *CSDCorrections* yields 3D CSDs expressed as a function of L, we expressed the CSDs as a function of S with additional corrections, because the latter is relatively insensitive to changes in crystal growth rate and thus more obviously shows changes in nucleation rate during magma ascent (Okumura et al., 2022a). We followed the correction procedure of Okumura et al. (2022a), but reduced the correction for sectioning effects in tracht-specific CSDs (see Online Resource 2), because the nature of the datasets and thus the correction assumption differed from those of Okumura et al. (2022a). The CSDs were plotted on logarithmic size intervals with five intervals per decade larger than 100 nm (i.e., each interval is $10^{0.2}$ times as large as the next smaller interval: $10^{2.0}$–$10^{2.2}$ nm, $10^{2.2}$–$10^{2.4}$ nm, $10^{2.4}$–$10^{2.6}$ nm…).

Results

Tracht-specific CSDs

Most of groundmass pyroxenes in the pumice samples were prismatic and those in the sub-Plinian samples tended to be more elongated than those in the Vulcanian samples

(Table 2, Figs. S2 and S3 in Online Resource 3). Most pyroxenes exhibited hexagonal or octagonal shapes in the polished sections, and all pumice samples contained these trachts and heptagonal one (Figs. 2 and 3; Table 3). There were no obvious differences in the spatial distributions of the trachts among the samples. Figure 3 shows the groundmass pyroxene CSDs for the six pumice samples. As reported by Mujin et al. (2017), the conventional CSDs (i.e., including all crystal trachts) were concave up in all samples (black lines in Fig. 3). In addition, those of the low-SiO_2 samples (i.e., sP_a–c and V-L) had steeper slopes in the size range $S < 2$ μm than those of the high-SiO_2 Vulcanian samples (i.e., V-H_a and V-H_b).

Figure 3 also shows tracht-specific CSDs for octagonal, heptagonal, and hexagonal cross sections. The size distributions of the trachts exhibited distinct trends, and the proportions of trachts within each sample (Table 3) depended on the type of pumice (i.e., low-SiO_2 vs. high-SiO_2). The low-SiO_2 pumice samples (sP_a–c and V-L) were characterized by coexisting hexagonal nanolites and octagonal crystals (Fig. 3a–c, f), whereas the high-SiO_2 pumice samples (V-H_a and V-H_b) contained mostly octagonal crystals with far fewer hexagonal and heptagonal crystals (Fig. 3d, e). In both pumice types, octagonal crystals spanned wide size ranges, and their slopes were relatively gentler and similar to those of the conventional CSDs in the larger size range (*S* > 2 μm). More importantly, the size distributions of octagonal microlites were similar in all samples. In contrast, hexagonal crystals spanned narrower size ranges that were largely consistent with those at which the conventional CSDs showed steeper slopes (*S* < 2 μm; Fig. 3a–c, f). The slopes of the hexagonal CSDs were steeper than those of the octagonal CSDs and similar to those of the conventional nanolite (*S* < 1 μm) CSDs. The size ranges and slopes of heptagonal crystals were intermediate between those of the octagonal and hexagonal trachts, and their population densities were generally lower than those of both the octagonal and hexagonal trachts. Furthermore, the population densities of octagonal nanolites in low-SiO_2 samples were reduced compared to those in high-SiO_2 samples in response to the appearance of hexagonal nanolites.

Crystallographic analyses of groundmass pyroxenes

Figure 4 shows the 3D morphology and crystallographic axes of the large hexagonal pyroxene microlite in the dense fragment (V-L-djf). The hexagonal prism was elongated along its *c*-axis, consisted of {010} and {110} prismatic faces, and was truncated by a rough surface lacking any facet or distinct crystallographic index (the other end was polished away). Although the detail of this truncated surface was limited by the effective spatial resolution of the SR-XnCT images (~200 nm), we assume that the growth rate of this rough surface must have been larger than those of the relatively flat {010} and {110} surfaces to produce such an elongated crystal.

Figures 5–8 summarize our TEM observations of pyroxene nanolites and microlites in samples sP_a, V-H_a, and V-L. The above combinations of prismatic faces were confirmed in other groundmass pyroxenes by TEM analyses (Figs. 5–7). Octagonal crystals had an additional pair of {100} faces (Figs. 7, 8), and heptagons lacked {100} faces on one side. Cross-sectional shapes similarly corresponded to these combinations of plane indices in all samples observed.

Almost all crystals observed by TEM showed epitaxial parallel growth of Opx (*Pbca*) and Cpx composed of augite (Aug; *C*2/*c*) and pigeonite (Pgt; $P2_1/c$), as reported by Sharp et al. (1996) and Mujin et al. (2017). Figure 5 shows a typical texture observed in a pyroxene nanolite in sP_a. The SAED patterns (Fig. 5f–h) show that a pair of Cpx domains epitaxially attached to the (100) and ($\bar{1}$00) surfaces of Opx. In some crystals, the two epitaxial Cpx domains were in a twin relationship (Fig. 5f, h). The SAED patterns of Cpx domains sometimes showed weak reflections of $P2_1/c$ in addition to those of $C2/c$ (i.e., the *hkl* reflections of "$h + k$ = even"; Fig. 5f, h), indicating that Aug and Pgt exist both as fine exsolution lamellae (Fig. 5) and as distinct domains (Fig. 6). Rarely, distinct domains of Pgt and Aug formed parallel growth textures without Opx (Fig. 6).

As shown in the ADF-STEM images and compositional maps perpendicular to the *c*-axis (Figs. 5a–d, 6a–d, 7, and 8a–d), most of the observed groundmass pyroxenes showed compositional growth zoning with low-Mg# (=Mg/(Mg + Fe)) rims. The low-Mg# rims were approximately 10–300 nm wide. In the low-SiO_2 samples (sP_a and V-L), this zoning was common and was characterized by a distinct boundary between the core and rim. Moreover, this sharp rim tended to be enriched in Al and Ti, especially in low-Ca pyroxene phases (Figs. 5c, 6c, and 7c, g; quantitative data are reported in Online Resource 4). The zoning boundaries showed euhedral shapes. In most crystals, the zoning boundary was the same shape as their external tracht (Figs. 5 and 7); however, a few hexagonal crystals exhibited internal octagonal zoning boundaries (Fig. 6), indicating the extinction of {100} faces during growth. In contrast, pyroxenes in the high-SiO_2 sample (V-H_a) tended to have more diffuse rims (Fig. 8a–d), and in some crystals, especially nanolites, the low-Mg# rim was not discernible (Fig. 8e–h). Additionally, when low-Mg# rims were present in the high-SiO_2 sample, no obvious enrichment of Al and Ti was observed, in contrast to those in the low-SiO_2 samples (Fig. 8c, g).

Discussion

Interpretation of tracht-specific CSDs

The observed groundmass pyroxene textures differ between the low-SiO_2 and high-SiO_2 pumices, as summarized in Figure 9. Before investigating the syneruptive magma ascent paths, we first derive crystallization histories from the tracht-specific CSDs (Fig. 3).

The size ranges and population densities of groundmass pyroxene crystals differed according to their crystal tracht. Pyroxene microlites in all samples and most nanolites in the high-SiO_2 samples were characterized by the octagonal tracht (Fig. 3). In contrast, the hexagonal tracht dominated nanolites in the low-SiO_2 samples (Fig. 3a–c, f). Moreover, the population densities of the hexagonal nanolites exceeded those of octagonal crystals in the low-SiO_2 samples, and the CSD slopes of nanolites and hexagonal crystals were steeper than those of microlites and octagonal ones. This means that the production of the hexagonal tracht was accompanied by an accelerated increase in pyroxene nucleation rate, suggesting a high degree of effective undercooling (ΔT_{eff}, i.e., including cooling and the contribution from decompression-induced dehydration; e.g., Armienti et al. 1994; Marsh 1998; Okumura et al. 2022a). Indeed, the hexagonal tracht is reproduced at $\Delta T_{\mathrm{eff}} > 100$ °C in the decompression experiment of a dacitic magma (Okumura et al. 2022b; discussed in the following subsection).

It is difficult to exclude the possibility that the hexagonal and octagonal crystals originated from different magma batches based solely on the tracht-specific CSDs (Fig. 3). However, given the lack of any obvious difference in the spatial distributions of the different trachts among samples, it is plausible that a single magma batch underwent successive crystallization conditions. This interpretation is consistent with the hexagonal crystals showing internal octagonal zoning boundaries in the low-SiO_2 sample (Fig. 6).

In the case of the low-SiO_2 samples, and given this crystallization sequence in a single magma batch, the tracht-specific CSDs indicate that the octagonal tracht was favored during an early crystallization stage at depth, and that the crystallizing conditions then changed into those favoring the hexagonal tracht as the magma ascended into the shallow conduit (Fig. 3a–c, f). In this case, we assume that the larger microlites retained their octagonal tracht during shallow crystallization because, compared to nanolites, a larger-volume overgrowth is required to change their tracht to hexagonal. In contrast, some hexagonal pyroxenes, especially those 1–2 μm wide, must have originally been octagonal, as suggested by the distributions of heptagonal crystals (i.e., the transitional tracht between octagonal and hexagonal; Fig. 3) and the presence of hexagonal crystals with internal octagonal growth zoning (Fig. 6). Therefore, we note that the tracht-specific CSDs describe the final texture after quenching and could be strictly different from the nucleation history of each tracht.

In contrast to the low-SiO_2 samples, which are assumed to have experienced increasing ΔT_{eff}, the crystallization kinetics of the high-SiO_2 samples can be similar to that of single-step decompression/cooling experiments because the magma stagnated in the conduit prior to the Vulcanian eruptions (Suzuki et al. 2018). Arzilli et al. (2022) performed *in situ* 4D (3D + time) observation of cooling-induced crystallization in a hydrous trachybasaltic magma. After they imposed cooling in a single step, several nucleation events occurred through time; moreover, the time-evolutions of growth rate and the resultant sizes of the crystals were similar regardless of their nucleation timing. Since crystals can reach similar sizes while held at a certain ΔT_{eff} (Arzilli et al. 2022), the peak positions of the CSDs for the high-SiO_2 samples at slightly larger sizes (Fig. 3d, e; Okumura et al. 2022a) can be attributed to the quasi-single-step decompression path. Given the tracht-specific CSDs (Fig. 3d, e), the magma of the high-SiO_2 samples was held at the condition favoring the octagonal tracht through the crystallization history.

From the above, in the following subsections, we discuss the groundmass crystallization histories in two stages: early and late stages when microlites and nanolites nucleated in the deep and shallow parts of the volcanic conduit, respectively. The early stage for all samples and the late stage for the high-SiO_2 samples were octagon-dominant, whereas only the late stage for the low-SiO_2 samples was hexagon-dominant.

Factors controlling the tracht of groundmass pyroxenes

The tracht change of groundmass pyroxene crystals in hydrous dacite magma was previously investigated via single-step decompression experiments by Okumura et al. (2022b). Although they did not mention the plane indices of crystals, they found that the dominant groundmass pyroxene tracht changed from octagonal to hexagonal as the final pressure decreased and that pyroxenes in differentiated melts within 10 μm of plagioclase crystals were more likely to be hexagonal. They suggested that the pyroxene tracht was related to ΔT_{eff}: increasing ΔT_{eff} with decreasing final pressure and melt evolution due to plagioclase crystallization (Mujin et al. 2017) caused the tracht change from octagonal to hexagonal. The value of ΔT_{eff} for each experiment was estimated from the liquidus determined experimentally by Sekine et al. (1979), and their results showed that the tracht change occurred at $\Delta T_{\mathrm{eff}} = 90$–$110$ °C. Based on this correlation, the existence of hexagonal nanolites indicates that the late stage of pyroxene crystallization in the low-SiO_2 samples proceeded under high ΔT_{eff}, consistent with their high nucleation rates (Fig. 3) and elongated shapes (Table 2). Although the experienced ΔT_{eff} might be higher than the threshold value determined by the experiments of dacitic magma (Okumura et al.

2022b; $\Delta T_{\mathrm{eff}} \sim 100$ °C), the threshold ΔT_{eff} can be different in the andesitic magma of the Shinmoedake volcano because the melt composition and chemical diffusivity probably affect growth mechanisms and resultant crystal textures (e.g., Lofgren 1974; Sunagawa 1981; Hammer 2008; Mollo and Hammer 2017). For example, Cpx crystals are governed by interface-controlled growth at $\Delta T_{\mathrm{eff}} < 112$ °C in a hydrous basaltic-andesite magma (Shea and Hammer 2013), whereas they exhibit diffusion-controlled growth texture at $\Delta T_{\mathrm{eff}} \geq 30$ °C in hydrous basaltic magmas (Moschini et al. 2021; Arzilli et al. 2022). Given the difference in threshold ΔT_{eff} for the growth mechanisms, the threshold for the tracht change might similarly depend on melt compositions. Therefore, further experiments using andesitic magma are required to estimate the accurate value of ΔT_{eff} during the ascent.

Moreover, we confirmed that the octagonal tracht comprises {100}, {010}, and {110} prismatic faces and that the change to the hexagonal one by losing {100} faces (Figs. 4–8). These results indicate that the relative growth rates of {100} faces become faster than those of other prismatic faces under high ΔT_{eff} until the faces disappear. On the other hand, relationships between the degree of cooling-induced undercooling, ΔT, and relative growth rate for different faces of Cpx were previously investigated by Kouchi et al. (1983). They conducted cooling-induced crystallization experiments in the system $CaMgSi_2O_6$–$CaTiAl_2O_6$. In the ΔT range where Cpx crystals had smooth surfaces, their results showed that the order of the growth rates of Cpx faces was (110) < (010) < (100) < ($\bar{1}$11) and that the differences between the growth rates increased with increasing ΔT. On the other hand, the crystallization kinetics likely differ between their melt of Cpx composition and a multi-component magmatic system in general (Sunagawa 1981, 2005), and the difference should be more significant than that between different magmas mentioned above. Nevertheless, we assume that their results except the quantitative values of ΔT are qualitatively applicable to crystallization during the 2011 Shinmoedake eruption because the growth mechanism, i.e., interface-controlled growth, is essentially the same in both systems, as suggested by the smooth prismatic faces of the pyroxene crystals studied herein.

During interface-controlled growth, the key process limiting the growth rate is not mass transfer through the melt towards the crystal surface, but the attachment of growth components on the surface (Hammer 2008). The attachment energy E_{att} strongly affects the relative growth rates of different crystallographic faces and thus the resultant crystal tracht (e.g., Hartman and Perdok 1955a, b; Hartman and Bennema 1980; Duan et al. 2010). E_{att} on faces {*hkl*} is defined as the bond energy released per structural unit when a growth unit (i.e., a layer of crystal on the {*hkl*} face) attaches to the crystal surface. In general, crystallographic faces with higher E_{att} have faster relative growth rates and thus lower morphological importance (e.g., Hartman and Perdok 1955a, b; Hartman and Bennema 1980; Liu and Bennema 1996). Van Panhuys-Sigler and Hartman (1981) calculated E_{att} for Cpx crystal faces based on periodic bond chain theory (Hartman and Perdok 1955a) and found that E_{att} for different faces follows the order (110) < (010) < (100) < ($\bar{1}$11), consistent with the growth rates determined experimentally by Kouchi et al (1983). Their calculations also showed that, assuming that the relative growth rate is proportional to E_{att}, the growth form of augite is the hexagonal tracht with {010} and {110} prismatic faces.

From the above evidence, among the important prismatic faces of Cpx, {100} faces are the most likely to disappear because of the crystallographic structure, and an increase in ΔT_{eff} further promotes their disappearance. Given the order of E_{att} for different faces, an additional increase in ΔT_{eff} may also make {010} faces disappear, resulting in a parallelogrammatic tracht composed of {110} faces as observed in pumice from the 1914

Plinian eruption of the Sakurajima volcano (Okumura et al. 2022b).

This same mechanism depending on ΔT_{eff} and the order of E_{att} for different faces can explain why the groundmass pyroxenes in the sub-Plinian samples are more elongated than those in the Vulcanian ones (Table 2). There are two factors that can increase ΔT_{eff}: magma ascent rate and melt evolution by crystallization. It is plausible that the magma ascent rate was faster during the sub-Plinian than the Vulcanian eruptions because textural analyses of pyroclasts and geophysical observations indicate that the magma stagnated in the conduit prior to the Vulcanian eruptions (Suzuki et al. 2018). The rapid ascent during the sub-Plinian eruptions should have involved large ΔT_{eff} due to decompression-induced dehydration and possibly cooling. Therefore, late crystallization in the low-SiO_2 samples (i.e., the sub-Plinian pumices and one Vulcanian pumice) should have occurred under the largest ΔT_{eff} during the 2011 eruptive activity; hence the occurrence of the hexagonal tracht in those samples (Fig. 3).

In contrast, plagioclase crystallization causes melt evolution and may increase the degree of supersaturation for pyroxene in the melt (Mujin et al. 2017). In the case of the 2011 Shinmoedake eruption, the whole-rock compositions (SiO_2 = 57.3–58.4 wt%; Suzuki et al. 2013) and the bulk groundmass compositions excluding phenocrysts (SiO_2 = 62–65 wt%; Mujin and Nakamura 2020) of the brown-gray pumices were similar regardless of the pumice type. Therefore, the difference in glass composition (low-SiO_2 vs. high-SiO_2) is due to crystallization differentiation from the initial melt (i.e., the bulk groundmass) during the ascent (Mujin and Nakamura 2020). The degrees of plagioclase crystallization and melt evolution were highest in the late crystallization stage of the high-SiO_2 samples, followed in order by the late stage of the low-SiO_2 samples and the early stages of both samples (Mujin and Nakamura 2014, 2020; Suzuki et al. 2018). Therefore, in terms of melt evolution, nanolites in the high-SiO_2 samples are the most likely to be hexagonal. However, our results show that only the late crystallization of the low-SiO_2 samples was hexagon-dominant (Fig. 3). Accordingly, we conclude that melt evolution is not the main factor that caused the tracht change. Therefore, in the case of the 2011 Shinmoedake eruption, the tracht change resulted from the high ΔT_{eff} associated with rapid magma ascent through the shallow conduit.

Crystallization conditions and the timing of growth zoning

Growth zoning records the ascent paths of individual crystals after their nucleation. In general, normal Mg# zoning could reflect evolution of the melt, cooling (e.g., Lindsley 1983; Lofgren et al. 2006; Putirka 2008), and/or reduced oxygen fugacity (Hammer 2006), which can result from sulfur degassing during decompression (e.g., Burgisser and Scaillet 2007; Blundy et al. 2008; Okumura et al. 2021). In addition, the enrichment of pyroxene in Al indicates rapid growth (e.g., Dymek and Gromet 1984; Mollo et al. 2013; Masotta et al. 2020). In our low-SiO_2 samples, the groundmass pyroxene crystals had low-Mg# and Al-rich rims with distinct boundaries (Figs. 5–7), indicating their rapid growth after an abrupt change in the surrounding conditions. In other words, their sharp rims formed during rapid ascent through the shallowest and possibly cold part of the conduit, perhaps in a gas-pyroclast flow after magma fragmentation (see the next paragraph, Fig. 10). In contrast, the gradual Mg# zoning without any associated Al enrichment in the high-SiO_2 samples (Fig. 8) indicates slow ascent or stagnation. These inferences are consistent with our above interpretation of the tracht-specific CSDs.

The time scale for the formation of the sharply zoned rims in the low-SiO_2 samples can be estimated based on the growth rate of pyroxene. Although data on pyroxene growth rates in dacitic to rhyolitic melts are lacking, pyroxene growth rates on the order of 10^{-7}–10^{-5} mm/s (time averages over the experimental durations) have been reported from several crystallization experiments in andesitic (Shea and Hammer 2013) and trachybasaltic melts (Pontesilli et al. 2019; Masotta et al. 2020). Moreover, *in-situ* observations of pyroxene crystallization in trachybasalt revealed that the instantaneous growth rate of pyroxene can reach 1×10^{-4} mm/s (Arzilli et al. 2019, 2022; Le Gall et al. 2021). Assuming that the instantaneous growth rate is slower in andesitic-dacitic melt than in trachybasaltic melt, with a maximum value of 1×10^{-5} mm/s, a 100 nm thick rim should form in 10 s. For comparison, the duration between magma fragmentation and quenching (or vitrification) can be estimated as follows. Numerical simulations (Suzuki and Koyaguchi 2013, 2015) indicate that high temperatures in the eruption column can be maintained to up to a few kilometers above the fragmentation level, corresponding to flight times of a few tens of seconds at the sound velocity of the gas-pyroclast mixture (e.g., 134 m/s; Suzuki and Koyaguchi 2013). In cold air (0 °C), a spherical pumice clast 1 cm in diameter would quench from an initial temperature of 950 °C (Suzuki et al. 2013; Tomiya et al. 2013) by conductive cooling within 10 s at a thermal diffusivity of 3.2×10^{-7} m^2/s (Bagdassarov and Dingwell 1994). Therefore, it could take several tens of seconds for a pumice clast to quench in an eruption plume, which is comparable to the minimum timescale of the rim formation. Further investigation of pyroxene growth rates in dacitic and rhyolitic melts are required to verify whether the sharply zoned rims observed herein formed after magma fragmentation.

Finally, we note that the change from octagon-dominant to hexagon-dominant conditions preceded the formation of the low-Mg# rims (Fig. 10) because most hexagonal crystals had hexagonal zoning boundaries (Fig. 5). Therefore, the tracht change probably resulted from the ascent condition prior to fragmentation (Fig. 10).

Implications

Based on the pyroxene trachts, we interpret the magma ascent paths during the 2011 Shinmoedake eruption (Fig. 10). The tracht and size distributions of the pyroxene microlites (i.e., >1 μm wide) are almost the same in all samples (Fig. 3), indicating that the ascent conditions deeper in the conduit were identical for both the sub-Plinian and

Vulcanian eruptions. Consistently, the CSDs of plagioclase microlites (Mujin and Nakamura 2014; Mujin et al. 2017; Suzuki et al. 2018) were almost the same, regardless of eruptive style.

In the shallow conduit, the magma ascent conditions diverged according to eruption style: the tracht-specific CSDs of the low-SiO_2 samples (Fig. 3a–c, f) clearly demonstrate differences in the crystallization kinetics (i.e., nucleation and growth) of nanolites and microlites. The magma accelerated in the shallow conduit during the sub-Plinian eruptions, increasing ΔT_{eff} enough to produce hexagonal nanolites before magma fragmentation. Their sharply zoned low-Mg# rims then formed in the shallowest part of the conduit or during cooling within the plume. In contrast, the magma ascended slowly or stagnated in the shallow conduit prior to Vulcanian eruptions, where the relatively slow growth of pyroxene resulted in gradually zoned rims, when present. This prolonged crystallization period maintained ΔT_{eff} within octagon-dominant conditions, and the final rapid ascent accompanied by the fragmentation produced a small number of hexagonal nanolites.

In addition, the CSDs of the low-SiO_2 Vulcanian pumice (V-L; Fig. 3f) are similar to those of the sub-Plinian pumice (Fig. 3a–c), indicating that a portion of the magma erupted during the Vulcanian eruption followed almost the same ascent paths just prior to the fragmentation as those during the sub-Plinian eruptions (Fig. 10). Similarly, Matsumoto and Geshi (2021) reported the co-existence of vesicular low-SiO_2 particles and poorly vesiculated high-SiO_2 particles in ash collected during the 2018 eruption of Shinmoedake, which was accompanied by lava effusion and frequent small explosions. They attributed these different textures to the simultaneous eruption of magmas with different decompression paths: (1) rapid ascent from deeper parts of the conduit and (2) slow ascent or stagnation in the shallow conduit. Therefore, the rapid ascent of deeper magma may not be exclusive to sub-Plinian eruptions at Shinmoedake, but may also be involved in the Vulcanian eruptions.

Our observations have demonstrated the applicability of pyroxene tracht analyses to the investigation of magma ascent paths in the conduit. The tracht-specific CSDs recorded the acceleration of magma batches in the shallow conduit, and associated growth zoning recorded the conditions in the surrounding magma. In addition, the tracht analyses can be applicable even to glassy pyroclasts with few groundmass crystals resulting from considerably fast ascent. Therefore, pyroxene tracht is expected to be a clue to elucidate magma dynamics in shallow conduits and those on short time scales just prior to eruptions. Experiments reproducing the observed tracht-specific CSDs and growth zonations of groundmass pyroxene crystals will provide information on time-evolution of magma conditions (e.g., temperature, pressure, ΔT_{eff}) during syneruptive ascent. This approach is probably applicable even to glassy pyroclasts produced by explosive eruptions and will elucidate the mechanisms controlling eruptive style during syneruptive ascent in shallow conduits.

Acknowledgments

The authors thank Kentaro Uesugi, Akihisa Takeuchi, Masahiro Yasutake, and Tsukasa Nakano for help with the SR-XnCT experiments, and Junya Matsuno for help with image processing. We thank Fabio Arzilli, Francisco Cáceres, and Maurizio Petrelli for many constructive comments that significantly improved our manuscript. The SR-XnCT experiments at SPring-8 in this study were conducted under proposal nos. 2018A1373, 2018B1298, 2019A0166, 2019B0166, and 2020A0166. This work was supported by JST

SPRING, Grant Number JPMJSP2110 to SO and JSPS KAKENHI Grant Number JP16H06348 and JP20H00198 to AM, JP15H05695 to AT and JP20H00205 to AT and AM.

References

Armienti, P. (2008) Decryption of Igneous Rock Textures: Crystal Size Distribution Tools. Reviews in Mineralogy and Geochemistry, 69, 623–649. https://doi.org/10.2138/rmg.2008.69.16

Armienti, P., Pareschi, M.T., Innocenti, F., and Pompilio, M. (1994) Effects of magma storage and ascent on the kinetics of crystal growth. Contributions to Mineralogy and Petrology, 115, 402–414. https://doi.org/10.1007/BF00320974

Arzilli, F., and Carroll, M.R. (2013) Crystallization kinetics of alkali feldspars in cooling and decompression-induced crystallization experiments in trachytic melt. Contributions to Mineralogy and Petrology, 166, 1011–1027. https://doi.org/10.1007/s00410-013-0906-1

Arzilli, F., Agostini, C., Landi, P., Fortunati, A., Mancini, L., and Carroll, M.R. (2015) Plagioclase nucleation and growth kinetics in a hydrous basaltic melt by decompression experiments. Contributions to Mineralogy and Petrology, 170, 55. https://doi.org/10.1007/s00410-015-1205-9

Arzilli, F., Piochi, M., Mormone, A., Agostini, C., and Carroll, M.R. (2016a) Constraining pre-eruptive magma conditions and unrest timescales during the Monte Nuovo eruption (1538 AD; Campi Flegrei, Southern Italy): integrating textural and CSD results from experimental and natural trachy-phonolites. Bulletin of Volcanology, 78, 72. https://doi.org/10.1007/s00445-016-1062-z

Arzilli, F., Polacci, M., Landi, P., Giordano, D., Baker, D.R., and Mancini, L. (2016b) A novel protocol for resolving feldspar crystals in synchrotron X-ray microtomographic images of crystallized natural magmas and synthetic analogs. American Mineralogist, 101, 2301–2311. https://doi.org/10.2138/am-2016-5788

Arzilli, F., La Spina, G., Burton, M.R., Polacci, M., Le Gall, N., Hartley, M.E., Di Genova, D., Cai, B., Vo, N.T., Bamber, E.C., and others. (2019) Magma fragmentation in highly explosive basaltic eruptions induced by rapid crystallization. Nature Geoscience, 12, 1023–1028. https://doi.org/10.1038/s41561-019-0468-6

Arzilli, F., Stabile, P., Fabbrizio, A., Landi, P., Scaillet, B., Paris, E., and Carroll, M.R.

(2020) Crystallization kinetics of alkali feldspar in peralkaline rhyolitic melts: implications for Pantelleria volcano. Frontiers in Earth Science, 8, 177. https://doi.org/10.3389/feart.2020.00177

Arzilli, F., Polacci, M., La Spina, G., Le Gall, N., Llewellin, E.W., Brooker, R.A., Torres-Orozco, R., Di Genova, D., Neave, D.A., Hartley, M.E., and others. (2022) Dendritic crystallization in hydrous basaltic magmas controls magma mobility within the Earth's crust. Nature Communications, 13, 3354. https://doi.org/10.1038/s41467-022-30890-8

Bagdassarov, N., and Dingwell, D. (1994) Thermal properties of vesicular rhyolite. Journal of Volcanology and Geothermal Research, 60, 179–191. https://doi.org/10.1016/0377-0273(94)90067-1

Befus, K.S., and Andrews, B.J. (2018) Crystal nucleation and growth produced by continuous decompression of Pinatubo magma. Contributions to Mineralogy and Petrology, 173, 92. https://doi.org/10.1007/s00410-018-1519-5

Blundy, J., Cashman, K.V., and Berlo, K. (2008) Evolving magma storage conditions beneath Mount St. Helens inferred from chemical variations in melt inclusions from the 1980–1986 and current (2004–2006) eruptions. In D.R. Sherrod, W.E. Scott, and P.H. Stauffer, Ed., A Volcano Rekindled: The Renewed Eruption of Mount St. Helens, 2004-2006, p. 755–790. U.S. Geological Survey, Washington. https://doi.org/10.3133/pp175033

Brugger, C.R., and Hammer, J.E. (2010a) Crystallization kinetics in continuous decompression experiments: implications for interpreting natural magma ascent processes. Journal of Petrology, 51, 1941–1965. https://doi.org/10.1093/petrology/egq044

Brugger, C.R., and Hammer, J.E. (2010b) Crystal size distribution analysis of plagioclase in experimentally decompressed hydrous rhyodacite magma. Earth and Planetary Science Letters, 300, 246–254. https://doi.org/10.1016/j.epsl.2010.09.046

Bruns, S., Stipp, S.L.S., and Sørensen, H.O. (2017) Looking for the signal: A guide to iterative noise and artefact removal in X-ray tomographic reconstructions of porous geomaterials. Advances in water resources, 105, 96–107. https://doi.org/10.1016/j.advwatres.2017.04.020

Burgisser, A., and Scaillet, B. (2007) Redox evolution of a degassing magma rising to the surface. Nature, 445, 194–197. https://doi.org/10.1038/nature05509

Cashman, K.V. (1992) Groundmass crystallization of Mount St. Helens dacite, 1980–1986: a tool for interpreting shallow magmatic processes. Contributions to Mineralogy and Petrology, 109, 431–449. https://doi.org/10.1007/BF00306547

Cashman, K.V., and Marsh, B.D. (1988) Crystal size distribution (CSD) in rocks and the kinetics and dynamics of crystallization II: Makaopuhi lava lake. Contributions to Mineralogy and Petrology, 99, 292–305. https://doi.org/10.1007/BF00375363

Cassidy, M., Manga, M., Cashman, K., and Bachmann, O. (2018) Controls on explosive-effusive volcanic eruption styles. Nature communications, 9, 2839. https://doi.org/10.1038/s41467-018-05293-3

Castro, J.M., and Dingwell, D.B. (2009) Rapid ascent of rhyolitic magma at Chaitén volcano, Chile. Nature, 461, 780–783. https://doi.org/10.1038/nature08458

Cloetens, P., Pateyron-Salomé, M., Buffiere, J.Y., Peix, G., Baruchel, J., Peyrin, F., and Schlenker, M. (1997). Observation of microstructure and damage in materials by phase sensitive radiography and tomography. Journal of Applied Physics, 81, 5878–5886. https://doi.org/10.1063/1.364374

Couch, S., Sparks, R.S.J., and Carroll, M.R. (2003) The kinetics of degassing-induced crystallization at Soufriere Hills Volcano, Montserrat. Journal of Petrology, 44, 1477–1502. https://doi.org/10.1093/petrology/44.8.1477

Donaldson, C.H. (1976) An experimental investigation of olivine morphology. Contributions to Mineralogy and Petrology, 57, 187–213. https://doi.org/10.1007/BF00405225

Duan, X., Wei, C., Liu, Y., and Pei, C. (2010) A molecular dynamics simulation of solvent effects on the crystal morphology of HMX. Journal of Hazardous Materials, 174, 175–180. https://doi.org/10.1016/j.jhazmat.2009.09.033

Dymek, R.F., and Gromet, L.P. (1984) Nature and origin of orthopyroxene megacrysts from the St-Urbain anorthosite massif, Quebec. The Canadian Mineralogist, 22, 297–326.

First, E.C., Leonhardi, T.C., and Hammer, J.E. (2020) Effects of superheating magnitude on olivine growth. Contributions to Mineralogy and Petrology, 175, 13. https://doi.org/10.1007/s00410-019-1638-7

Franke, W.A. (1989) Tracht and habit of synthetic minerals grown under hydrothermal conditions. European Journal of Mineralogy, 1, 557–566.

Giuliani, L., Iezzi, G., Vetere, F., Behrens, H., Mollo, S., Cauti, F., Ventura, G., and Scarlato, P. (2020) Evolution of textures, crystal size distributions and growth rates of plagioclase, clinopyroxene and spinel crystallized at variable cooling rates from a mid-ocean ridge basaltic melt. Earth-Science Reviews, 204, 103165. https://doi.org/10.1016/j.earscirev.2020.103165

Gonnermann, H.M., and Manga, M. (2007) The fluid mechanics inside a volcano. Annual Review of Fluid Mechanics, 39, 321–356. https://doi.org/10.1146/annurev.fluid.39.050905.110207

Hammer, J.E. (2006) Influence of fO_2 and cooling rate on the kinetics and energetics of Fe-rich basalt crystallization. Earth and Planetary Science Letters, 248, 618–637. https://doi.org/10.1016/j.epsl.2006.04.022

Hammer, J.E. (2008) Experimental studies of the kinetics and energetics of magma crystallization. In K.D. Putirka and F.J. Tepley III, Eds., Minerals, Inclusions and Volcanic Processes, 69, p. 9–60. Reviews in Mineralogy and Geochemistry, Mineralogical Society of America, Chantilly, Virginia.

https://doi.org/10.2138/rmg.2008.69.2

Hammer, J.E., and Rutherford, M.J. (2002) An experimental study of the kinetics of decompression-induced crystallization in silicic melt. Journal of Geophysical Research, 107, 1–23. https://doi.org/10.1029/2001JB000281

Hartman, P., and Bennema, P. (1980) The attachment energy as a habit controlling factor: I. Theoretical considerations. Journal of Crystal Growth, 49, 145–156. https://doi.org/10.1016/0022-0248(80)90075-5

Hartman, P., and Perdok, W.G. (1955a) On the relations between structure and morphology of crystals. I. Acta Crystallographica, 8, 49–52. https://doi.org/10.1107/S0365110X55000121

Hartman, P., and Perdok, W.G. (1955b) On the relations between structure and morphology of crystals. II. Acta Crystallographica, 8, 521–524. https://doi.org/10.1107/S0365110X55001679

Higgins, M.D. (2000) Measurement of crystal size distributions. American Mineralogist, 85, 1105–1116. https://doi.org/10.2138/am-2000-8-901

Kato, K., and Yamasato, H. (2013) The 2011 eruptive activity of Shinmoedake volcano, Kirishimayama, Kyushu, Japan—overview of activity and volcanic alert level of the Japan meteorological agency—. Earth, Planets and Space, 65, 489–504. https://doi.org/10.5047/eps.2013.05.009

Kouchi, A., Sugawara, Y., Kashima, K., and Sunagawa, I. (1983) Laboratory growth of sector zoned clinopyroxenes in the system $CaMgSi_2O_6$–$CaTiAl_2O_6$. Contributions to Mineralogy and Petrology, 83, 177–184. https://doi.org/10.1007/BF00373091

Kozono, T., Ueda, H., Ozawa, T., Koyaguchi, T., Fujita, E., Tomiya, A., and Suzuki, Y.J. (2013) Magma discharge variations during the 2011 eruptions of Shinmoe-dake volcano, Japan, revealed by geodetic and satellite observations. Bulletin of volcanology, 75, 695. https://doi.org/10.1007/s00445-013-0695-4

La Spina, G., Burton, M., and Arzilli, F. (2016) Role of syn-eruptive plagioclase disequilibrium crystallization in basaltic magma ascent dynamics. Nature communications, 7, 13402. https://doi.org/10.1038/ncomms13402

La Spina, G., Arzilli, F., Llewellin, E.W., Burton, M.R., Clarke, A.B., Vitturi, M.D.M., Polacci, M., Hartley, M.E., Di Genova, D., and Mader, H.M. (2021) Explosivity of basaltic lava fountains is controlled by magma rheology, ascent rate and outgassing. Earth and Planetary Science Letters, 553, 116658. https://doi.org/10.1016/j.epsl.2020.116658

Le Gall, N., Arzilli, F., La Spina, G., Polacci, M., Cai, B., Hartley, M.E., Vo, N.T., Atwood, R.C., Di Genova, D., Nonni, S., and others. (2021) In situ quantification of crystallisation kinetics of plagioclase and clinopyroxene in basaltic magma: Implications for lava flow. Earth and Planetary Science Letters, 568, 117016. https://doi.org/10.1016/j.epsl.2021.117016

Lindsley, D.H. (1983) Pyroxene thermometry. American Mineralogist, 68, 477–493.

Liu, X.Y., and Bennema, P. (1996) Theoretical consideration of the growth morphology of crystals. Physical Review B, 53, 2314–2325. https://doi.org/10.1103/PhysRevB.53.2314

Lofgren, G. (1974) An experimental study of plagioclase crystal morphology; isothermal crystallization. American Journal of Science, 274, 243–273.

Lofgren, G (1980) Experimental studies on the dynamic crystallization of silicate melts. In R.B. Hargraves, Ed., Physics of magmatic processes, p. 487–551. Princeton University Press, Princeton.

Lofgren, G.E., Huss, G.R., and Wasserburg, G.J. (2006) An experimental study of trace-element partitioning between Ti-Al-clinopyroxene and melt: Equilibrium and kinetic effects including sector zoning. American Mineralogist, 91, 1596–1606. https://doi.org/10.2138/am.2006.2108

Mader, H.M., Llewellin, E.W., and Mueller, S.P. (2013) The rheology of two-phase magmas: A review and analysis. Journal of Volcanology and geothermal Research, 257, 135–158. https://doi.org/10.1016/j.jvolgeores.2013.02.014

Mancini, L., Reinier, E., Cloetens, P., Gastaldi, J., Härtwig, J., Schlenker, M., and Baruchel, J. (1998) Investigation of structural defects and inhomogeneities in Al-Pd-Mn icosahedral quasicrystals by combined synchrotron X-ray topography and phase radiography. Philosophical Magazine A, 78, 1175–1194. https://doi.org/10.1080/01418619808239982

Mangler, M.F., Humphreys, M., Wadsworth, F.B., Iveson, A.A., and Higgins, M.D. (2022) Variation of plagioclase shape with size in intermediate magmas: a window into incipient plagioclase crystallisation. Contributions to Mineralogy and Petrology, 177, 64. https://doi.org/10.1007/s00410-022-01922-9

Marsh, B.D. (1998) On the interpretation of crystal size distributions in magmatic systems. Journal of Petrology, 39, 553–599. https://doi.org/10.1093/petroj/39.4.553

Masotta, M., Pontesilli, A., Mollo, S., Armienti, P., Ubide, T., Nazzari, M., and Scarlato, P. (2020) The role of undercooling during clinopyroxene growth in trachybasaltic magmas: Insights on magma decompression and cooling at Mt. Etna volcano. Geochimica et Cosmochimica Acta, 268, 258–276. https://doi.org/10.1016/j.gca.2019.10.009

Matsumoto, K., and Geshi, N. (2021) Shallow crystallization of eruptive magma inferred from volcanic ash microtextures: a case study of the 2018 eruption of Shinmoedake volcano, Japan. Bulletin of Volcanology, 83, 31. https://doi.org/10.1007/s00445-021-01451-6

Matsumoto, M., Tsuchiyama, A., Nakato, A., Matsuno, J., Miyake, A., Kataoka, A., Ito, M., Tomioka, N., Kodama, Y., Uesugi, K., Takeuchi, A., Nakano, T., and Vaccaro, E. (2019) Discovery of fossil asteroidal ice in primitive meteorite Acfer 094. Science Advances, 5, eaax5078. https://doi.org/10.1126/sciadv.aax5078

Miyake, A., Matsuno, J., and Toh, S. (2014) Sample preparation toward seamless 3D imaging technique from micrometer to nanometer scale. Microscopy, 63, i24–i25. https://doi.org/10.1093/jmicro/dfu055

Mollard, E., Martel, C., and Bourdier, J.L. (2012) Decompression-induced crystallization in hydrated silica-rich melts: empirical models of experimental plagioclase nucleation and growth kinetics. Journal of Petrology, 53, 1743–1766.

Mollo, S., and Hammer, J.E. (2017) Dynamic crystallization in magmas. In W. Heinrich and R. Abart, Eds., Mineral reaction kinetics: Microstructures, textures, chemical and isotopic signatures, 16, p. 373–418. European Mineralogical Union Notes in Mineralogy, European Mineralogical Union and Mineralogical Society of Great Britain and Ireland. https://doi.org/10.1180/EMU-notes.16.12

Mollo, S., Blundy, J.D., Iezzi, G., Scarlato, P., and Langone, A. (2013) The partitioning of trace elements between clinopyroxene and trachybasaltic melt during rapid cooling and crystal growth. Contributions to Mineralogy and Petrology, 166, 1633–1654. https://doi.org/10.1007/s00410-013-0946-6

Moschini, P., Mollo, S., Gaeta, M., Fanara, S., Nazzari, M., Petrone, C.M., and Scarlato, P.

(2021) Parameterization of clinopyroxene growth kinetics via crystal size distribution (CSD) analysis: Insights into the temporal scales of magma dynamics at Mt. Etna volcano. Lithos, 396–397, 106225. https://doi.org/10.1016/j.lithos.2021.106225

Mueller, S., Llewellin, E.W., and Mader, H.M. (2010) The rheology of suspensions of solid particles. Proceedings of the Royal Society A: Mathematical, Physical and Engineering Sciences, 466, 1201–1228. https://doi.org/10.1098/rspa.2009.0445

Mujin, M., and Nakamura, M. (2014) A nanolite record of eruption style transition. Geology, 42, 661–614. https://doi.org/10.1130/G35553.1

Mujin, M., and Nakamura, M. (2020) Late-stage groundmass differentiation as a record of magma stagnation, fragmentation, and rewelding. Bulletin of Volcanology, 82, 48. https://doi.org/10.1007/s00445-020-01389-1

Mujin, M., Nakamura, M., and Miyake, A. (2017) Eruption style and crystal size distributions: Crystallization of groundmass nanolites in the 2011 Shinmoedake eruption. American Mineralogist, 102, 2367–2380. https://doi.org/10.2138/am-2017-6052CCBYNCND

Nakada, S., Nagai, M., Kaneko, T., Suzuki, Y., and Maeno, F. (2013) The outline of the 2011 eruption at Shinmoe-dake (Kirishima), Japan. Earth, planets and space, 65, 475–488. https://doi.org/10.5047/eps.2013.03.016

Nakano, T., Nakashima, Y., Nakamura, K., and Ikeda, S. (2000) Observation and analysis of internal structure of rock using X-ray CT. Journal of Geological Society of Japan, 106, 363–378 (in Japanese). https://doi.org/10.5575/geosoc.106.363

Nakano, T., Tsuchiyama, A., Uesugi, K., Uesugi, M., and Shinohara, K. (2006) "Slice" -Softwares for basic 3-D analysis-. Available: http://www-bl20.spring8.or.jp/slice/. Japan Synchrotron Radiation Research Institute (JASRI), Hyogo.

Okumura, S., Ishibashi, H., Itoh, S., Suzumura, A., Furukawa, Y., Miwa, T., and Kagi, H. (2021) Decompression experiments for sulfur-bearing hydrous rhyolite magma: Redox evolution during magma decompression. American Mineralogist, 106, 216–225. https://doi.org/10.2138/am-2020-7535

Okumura, S.H., Mujin, M., Tsuchiyama, A., and Miyake, A. (2022a) 3D crystal size distributions of pyroxene nanolites from nano X-ray computed tomography: Improved correction of crystal size distributions from CSDCorrections for magma ascent dynamics in conduits. American Mineralogist, 107, 1766–1778. https://doi.org/10.2138/am-2022-8039

Okumura, S.H., Okumura, S., and Miyake, A. (2022b) Tracht change of groundmass pyroxene crystals in decompression experiments. Journal of Mineralogical and Petrological Sciences, 117, 211219. https://doi.org/10.2465/jmps.211219

Polacci, M., Arzilli, F., La Spina, G., Le Gall, N., Cai, B., Hartley, M.E., Di Genova, D., Vo, N.T., Nonni, S., Atwood, R.C. and others. (2018) Crystallisation in basaltic magmas revealed via *in situ* 4D synchrotron X-ray microtomography. Scientific Reports, 8, 8377. https://doi.org/10.1038/s41598-018-26644-6

Pontesilli, A., Masotta, M., Nazzari, M., Mollo, S., Armienti, P., Scarlato, P., and Brenna, M. (2019) Crystallization kinetics of clinopyroxene and titanomagnetite growing from a trachybasaltic melt: New insights from isothermal time-series experiments. Chemical Geology, 510, 113–129. https://doi.org/10.1016/j.chemgeo.2019.02.015

Putirka, K.D. (2008) Thermometers and barometers for volcanic systems. Reviews in Mineralogy and Geochemistry, 69, 61–120. https://doi.org/10.2138/rmg.2008.69.3

Rusiecka, M.K., and Martel, C. (2022) Nucleation delay in water-saturated rhyolite during decompression in shallow volcanic systems and its implications for ascent dynamics. Bulletin of Volcanology, 84, 61. https://doi.org/10.1007/s00445-022-01569-1

Rusiecka, M.K., Bilodeau, M., and Baker, D.R. (2020) Quantification of nucleation delay in magmatic systems: experimental and theoretical approach. Contributions to Mineralogy and Petrology, 175, 47. https://doi.org/10.1007/s00410-020-01682-4

Schupsky, J.P. (2020) Crystallisation of oxidic gasifier slags. Doctoral dissertation, Fakultät für Maschinenwesen, Rheinisch-Westfälische Technische Hochschule Aachen, Aachen. DOI:10.18154/RWTH-2020-10033

Sekine, T., Katsura, T., and Aramaki, S. (1979) Water saturated phase relations of some andesites with application to the estimation of the initial temperature and water pressure at the time of eruption. Geochimica et Cosmochimica Acta, 43, 1367–1376.

Seto, Y., and Ohtsuka, M. (2022) *ReciPro*: free and open-source multipurpose crystallographic software integrating a crystal model database and viewer, diffraction and microscopy simulators, and diffraction data analysis tools. Journal of Applied Crystallography, 55, 397–410. https://doi.org/10.1107/S1600576722000139

Shea, T., and Hammer, J.E. (2013) Kinetics of cooling- and decompression-induced crystallization in hydrous mafic-intermediate magmas. Journal of Volcanology and Geothermal research, 260, 127–145. https://doi.org/10.1016/j.jvolgeores.2013.04.018

Sunagawa, I. (1981) Characteristics of crystal growth in nature as seen from the morphology of mineral crystals. Bulletin de Minéralogie, 104, 81–87. https://doi.org/10.3406/bulmi.1981.7438

Sunagawa, I. (2005) Crystals: Growth, Morphology, and Perfection, 295 p. Cambridge University Press, New York.

Suzuki, Y., Yasuda, A., Hokanishi, N., Kaneko, T., Nakada, S., and Fujii, T. (2013) Syneruptive deep magma transfer and shallow magma remobilization during the 2011 eruption of Shinmoe-dake, Japan—Constraints from melt inclusions and phase equilibria experiments. Journal of Volcanology and Geothermal Research, 257, 184–204. https://doi.org/10.1016/j.jvolgeores.2013.03.017

Suzuki, Y., Maeno, F., Nagai, M., Shibutani, H., Shimizu, S., and Nakada, S. (2018) Conduit processes during the climactic phase of the Shinmoe-dake 2011 eruption (Japan): Insights into intermittent explosive activity and transition in eruption style of andesitic magma. Journal of Volcanology and Geothermal Research, 358, 87–104. https://doi.org/10.1016/j.jvolgeores.2018.02.008

Suzuki, Y.J., and Koyaguchi, T. (2013) 3D numerical simulation of volcanic eruption clouds during the 2011 Shinmoe-dake eruptions. Earth, Planets and Space, 65, 581–589. https://doi.org/10.5047/eps.2013.03.009

Suzuki, Y.J., and Koyaguchi, T. (2015) Effects of wind on entrainment efficiency in volcanic plumes. Journal of Geophysical Research: Solid Earth, 120, 6122–6140. https://doi.org/10.1002/2015JB012208

Takeuchi, A., Uesugi, K., and Suzuki, Y. (2009) Zernike phase-contrast x-ray microscope with pseudo-Kohler illumination generated by sectored (polygon) condenser plate. Journal of Physics: Conference Series, 186, 012020. https://doi.org/10.1088/1742-6596/186/1/012020

Tomiya, A., Miyagi, I., Saito, G., and Geshi, N. (2013) Short time scales of magma-mixing processes prior to the 2011 eruption of Shinmoedake volcano, Kirishima volcanic group, Japan. Bulletin of Volcanology, 75, 750. https://doi.org/10.1007/s00445-013-0750-1

Toramaru, A., Noguchi, S., Oyoshihara, S., and Tsune, A. (2008) MND(microlite number density) water exsolution rate meter. Journal of Volcanology and Geothermal Research, 175, 156–167. https://doi.org/10.1016/j.jvolgeores.2008.03.035

Tsuchiyama, A., Uesugi, M., Matsushima, T., Michikami, T., Kadono, T., Nakamura, T., Uesugi, K., Nakano, T., Sandford, S.A., Noguchi, R., and others. (2011) Three-dimensional structure of Hayabusa samples: origin and evolution of Itokawa regolith. Science, 333, 1125–1128. https://doi.org/10.1126/science.1207807

Tsuchiyama, A., Nakano, T., Uesugi, K., Uesugi, M., Takeuchi, A., Suzuki, Y., Noguchi, R., Matsumoto, T., Matsuno, J., Nagano, T., and others. (2013) Analytical dual-energy microtomography: A new method for obtaining three-dimensional phase images and its application to Hayabusa samples. Geochimica et Cosmochimica Acta, 116, 5–16. https://doi.org/10.1016/j.gca.2012.11.036

Ubide, T., and Kamber, B.S. (2018) Volcanic crystals as time capsules of eruption history. Nature Communications, 9, 326. https://doi.org/10.1038/s41467-017-02274-w

Uesugi, K., Takeuchi, A., and Suzuki, Y. (2006) Development of micro-tomography system with Fresnel zone plate optics at SPring-8. In U. Bonse, Ed., Proceedings of SPIE OPTICS + PHOTONICS, 6318, 63181F. International Society for Optics and Photonics, Bellingham, Washington. https://doi.org/10.1117/12.679822

Van Panhuys-Sigler, M., and Hartman, P. (1981) Morphologie théorique de certains pyroxenes déduite de la structure cristalline. Bulletin de Minéralogie, 104, 95–106 (in French). https://doi.org/10.3406/bulmi.1981.7441

Watanabe, M., and Williams, D.B. (2006) The quantitative analysis of thin specimens: a review of progress from the Cliff-Lorimer to the new ζ-factor methods. Journal of microscopy, 221, 89–109. https://doi.org/10.1111/j.1365-2818.2006.01549.x

Waters, L.E., Andrews, B.J., and Lange, R.A. (2015) Rapid crystallization of plagioclase phenocrysts in silicic melts during fluid-saturated ascent: phase equilibrium and decompression experiments. Journal of Petrology, 56, 981–1006.

https://doi.org/10.1093/petrology/egv025

Figure captions

Figure 1. Classification of crystal trachts. (**a**) Cross sections of groundmass pyroxene crystals were classified based on the number of faces between a given pair of parallel faces (indicated by yellow circles). (**b**) Incomplete shapes were classified similarly if a pair of parallel faces was present. (**c**) Individual segments of attached crystals were classified in a similar manner.

Figure 2. Backscattered electron (BSE) images of groundmass pyroxenes in (**a**) sub-Plinian pumice sP_a and (**b**) high-SiO_2 Vulcanian pumice V-H_a from the 2011 Shinmoedake eruption. These images were obtained by FE-SEM at an acceleration voltage of 10 kV. The tracht of each pyroxene crystal (i.e., octagonal, heptagonal, or hexagonal) is indicated by colored symbols (blue square, red diamond, and yellow triangle, respectively). Abbreviations: Pl, plagioclase; Px, pyroxene.

Figure 3. Tracht-specific CSDs of groundmass pyroxenes in the pumice samples. The conventional CSDs (i.e., including all trachts) are plotted in black for comparison. The size

range shown is from 0.10 to 6.31 μm in width (short-axis length). Open symbols with dashed lines represent data in size intervals where fewer than three crystals could be counted. (**a**–**c**) Sub-Plinian pumices; (**d**, **e**) high-SiO_2 Vulcanian pumices; (**f**) low-SiO_2 Vulcanian pumice.

Figure 4. 3D shape and plane indices of a relatively large hexagonal pyroxene microlite from the dense juvenile fragment V-L-djf. (**a**) The CT image and (**b**) 3D reconstruction acquired by SR-XnCT are shown with the crystallographic orientation as determined by EBSD analysis. The crystallographic indices of the prismatic faces are also noted in (**b**). The lower end of the crystal corresponds to the polished sample surface.

Figure 5. Representative internal texture of groundmass pyroxenes in the sub-Plinian pumice sP_a. The results of TEM analyses for a hexagonal nanolite in the sub-Plinian pumice sP_a are shown. (**a**) An ADF-STEM image and (**b**–**d**) Ca, Al, and Mg# (=Mg/(Mg + Fe) in mol) compositional maps, respectively, were obtained along the [001] zone axis. (**e**) A bright-field (BF) TEM image and (**f**–**h**) the SAED patterns of each domain were

obtained at another orientation. The medium gray shape around the pyroxene in (**e**) is the bright-field background, not an overgrowth. The two Cpx domains (**f, h**) have a twin relationship. Quantitative compositional data are reported in Supplementary Table S1. Abbreviations: Opx, orthopyroxene; Cpx, clinopyroxene.

Figure 6. Internal texture of a hexagonal pyroxene microlite in the sub-Plinian pumice sP_a. (**a**) An ADF-STEM image and (**b–d**) Ca, Al, and Mg# compositional maps, respectively, were obtained along the [001] zone axis, indicating the extinction of {100} faces during growth. (**e**) A schematic view of the zoning boundaries. The dashed lines represent the phase boundaries. (**f**) The SAED pattern of the Pgt domain at the center was obtained along the $[0\bar{1}2]$ zone axis. This crystallographic orientation is common in the crystal. Abbreviations: Pgt, pigeonite; Aug, augite.

Figure 7. Internal texture of (**a–d**) a microlite and (**e–h**) a nanolite in the low-SiO_2 Vulcanian pumice V-L. (**a**, **e**) The ADF-STEM images and (**b–d**, **f–h**) Ca, Al, and Mg# compositional maps, respectively, were obtained along the [001] zone axes. As shown in (**a**,

e), the two crystals have growth zonations of the same tracht as their external forms. The Cpx domains have a twin relationship in the microlite whereas those in the nanolite have the same crystallographic orientation. Abbreviations: Pgt, pigeonite; Opx, orthopyroxene; Cpx, clinopyroxene.

Figure 8. Internal texture of (**a**–**d**) a microlite and (**e**–**h**) a nanolite in the high-SiO_2 Vulcanian pumice V-H_a. (**a**, **e**) The ADF-STEM images and (**b**–**d**, **f**–**h**) Ca, Al, and Mg# compositional maps, respectively, were obtained along the [001] zone axes. Cpx domains in both crystals show twin relationships. Abbreviations: Pgt, pigeonite; Opx, orthopyroxene; Cpx, clinopyroxene.

Figure 9. Schematic illustration of the observed textures of groundmass pyroxenes. The typical textures of groundmass pyroxenes in (**a**) the low-SiO_2 and (**b**) the high-SiO_2 pumices are shown with their tracht-specific CSDs and internal textures. The tracht-specific CSDs of samples (**a**) sP_a and (**b**) V-H_a are provided as representative of each type of pumice. The inserted illustrations of pyroxene crystals show typical zoning patterns (blue:

low-Mg# rim) at the parts of the CSDs indicated by the arrows.

Figure 10. Schematic illustration of pyroxene crystallization kinetics and magma ascent paths during the 2011 Shinmoedake eruption. (**a**) Pressure–time paths and (**b**) ΔT_{eff}–time paths of the magmas that formed the low-SiO_2 and high-SiO_2 pumices are shown in orange and blue, respectively. The time evolution of the pyroxene texture is also shown in (**a**). The low-Mg# rims formed in the shallowest part of the conduit (blue shaded area in (**a**)). The vertical dashed line indicates the time when ΔT_{eff} exceeded the threshold between octagon-dominant and hexagon-dominant conditions (gray horizontal line in (**b**)) preceding the formation of the low-Mg# rims. The possible timings of magma fragmentation events are indicated by stars.

Tables

Table 1. Average chemical compositions of groundmass glasses (wt%).

	Sub-Plinian			Vulcanian			
	sP_a [a]	sP_b	sP_c	V-H_a [a]	V-H_b	V-L	V-L-djf
SiO_2	67.33 (41)	66.64 (27)	67.80 (35)	71.69 (21)	72.35 (29)	66.83 (45)	67.52 (61)
TiO_2	0.88 (5)	1.00 (4)	0.90 (5)	0.73 (4)	0.70 (4)	0.94 (6)	0.84 (8)
Al_2O_3	14.15 (26)	14.06 (21)	14.06 (16)	12.66 (9)	12.52 (18)	14.09 (23)	14.36 (20)
FeO	5.75 (25)	6.41 (16)	5.63 (19)	4.24 (13)	3.95 (13)	6.23 (30)	5.43 (45)
MnO	0.11 (5)	0.11 (5)	0.11 (4)	0.10 (4)	0.03 (5)	0.12 (5)	0.11 (4)
MgO	1.13 (8)	1.15 (9)	0.98 (5)	0.64 (3)	0.58 (6)	1.14 (11)	1.06 (10)
CaO	3.92 (19)	4.08 (10)	3.67 (13)	2.56 (9)	2.35 (11)	3.99 (15)	3.92 (19)
Na_2O	3.38 (10)	3.30 (10)	3.35 (8)	3.28 (12)	3.42 (9)	3.33 (9)	3.35 (8)
K_2O	3.24 (8)	3.12 (6)	3.37 (6)	3.93 (4)	3.98 (7)	3.22 (8)	3.29 (11)
P_2O_5	0.11 (5)	0.13 (5)	0.13 (4)	0.16 (4)	0.11 (8)	0.12 (4)	0.12 (4)
Total	100	100	100	100	100	100	100

NOTES: Each sample was analyzed in 50 distinct regions.

Values in parentheses are standard deviations.

Oxide concentrations were recalculated to total 100% by cation balance.

[a] Data from Okumura et al. (2022a) are corrected for losses of Na and K during the measurements.

Table 2. Conditions and results of SR-XnCT analyses.

Eruptive style	CT specimen	Voxel size (nm)	Number of crystals analyzed [a]	Average 3D aspect ratio		
				S	*I* [b]	*L* [b]
sub-Plinian	sP_a-1	40.00	74	1.0	1.4 [c] (6)	9.4 [c] (56)
	sP_a-2	24.70	103			
	sP_b	77.80	123	1.0	1.4 (3)	8.7 (46)
	sP_c	77.80	151	1.0	1.3 (2)	8.4 (44)
Vulcanian	V-H_a-1	33.86	47	1.0	1.3 [c] (4)	5.1 [c] (39)
	V-H_a-2	34.70	86			
	V-H_b	77.80	95	1.0	1.3 (4)	5.6 (40)
	V-L	77.80	163	1.0	1.4 (3)	6.5 (42)
	V-L-djf	34.70	1			

[a] Crystals smaller than 5 pixels in the shortest dimension *S* were excluded.

[b] Values in parentheses are standard deviations.

[c] Values averaged from two CT specimens; data from Okumura et al. (2022a).

Table 3. Parameters used in *CSDCorrections*.

Eruptive style	Sample	Number of regions	Analyzed area (excluding vesicles)		Number of crystal cross sections				3D aspect ratio	Roundness	Size scale length
			(μm^2)	(vesicle%) [b]	All	Octagon	Heptagon	Hexagon	*S*:*I*:*L*		(Bins per decade [c])
sub-Plinian	sP_a	1 [a]	20,077	57.3	793	83	34	385	1:1.4:9.4	0.8	5
	sP_b	2	15,291	37.2	1,037	167	59	399	1:1.4:8.7		
	sP_c	2	15,566	35.9	728	43	27	305	1:1.3:8.4		
Vulcanian	V-H_a	1 [a]	19,791	54.5	381	171	9	10	1:1.3:5.1		
	V-H_b	3	14,268	60.9	319	142	8	5	1:1.3:5.6		
	V-L	2	12,533	48.5	645	115	36	242	1:1.4:6.5		

[a] A single larger region comprising multiple BSE images (Okumura et al. 2022a).

[b] The percentage of vesicles in the analyzed rectangle area.

[c] Logarithmic base-10 size scale.

Figure 1

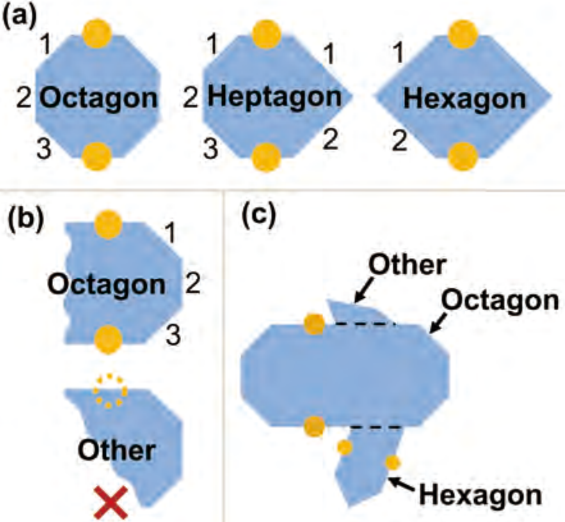
(a)
1
2 Octagon
3
1
1
2 Heptagon
3
2
1
Hexagon
2
(b)
1
Octagon
2
3
Other
(c)
Other
Octagon
Hexagon

Figure 2

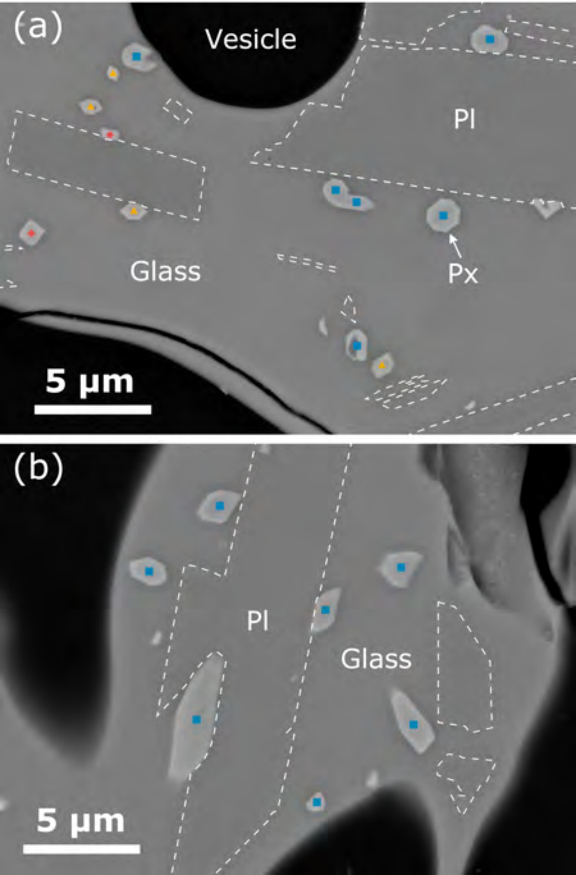

Figure 3

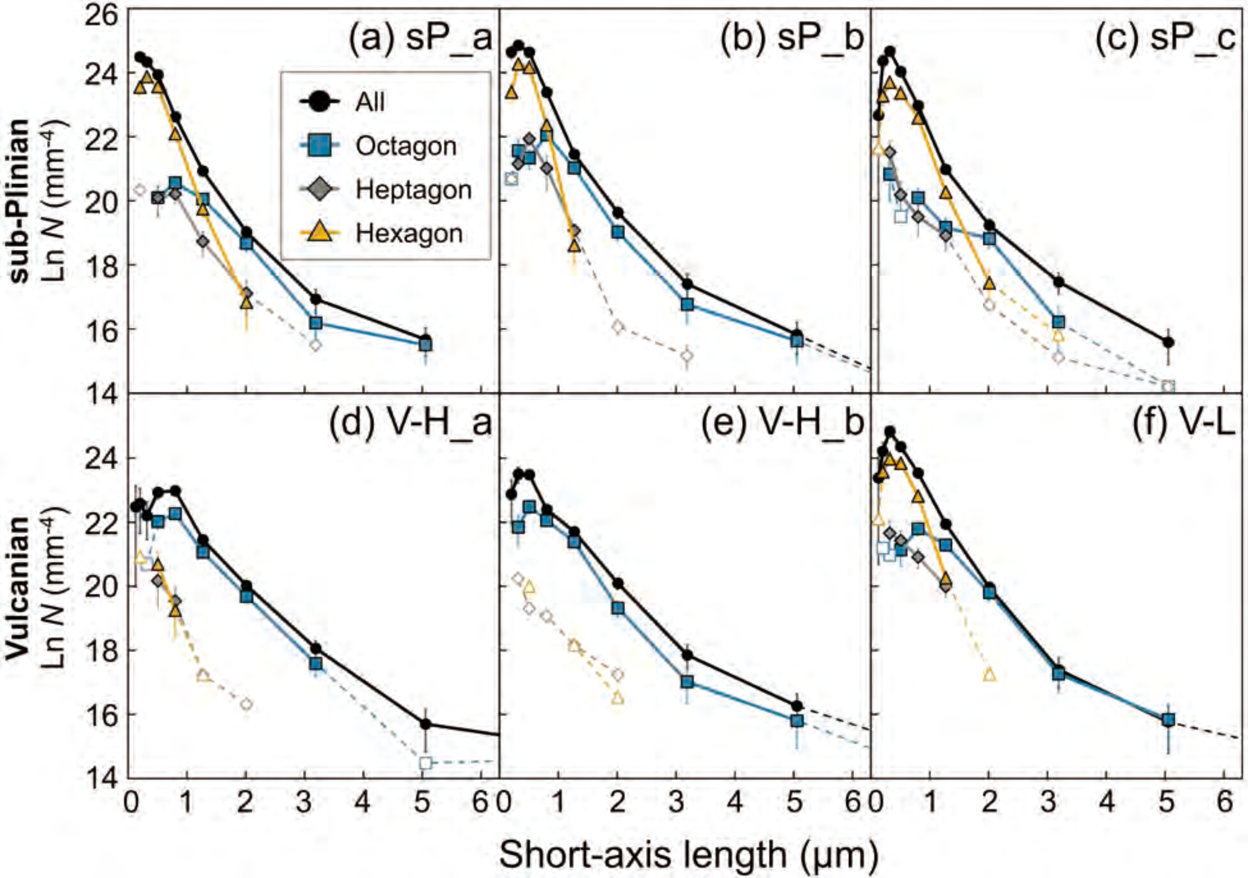
(a) sP_a
(b) sP_b
(c) sP_c
(d) V-H_a
(e) V-H_b
(f) V-L
All
Octagon
Heptagon
Hexagon
sub-Plinian
Vulcanian
Ln N (mm-4)
26
24
22
20
18
16
14
0
1
2
3
4
5
6
Short-axis length (μm)

Figure 4

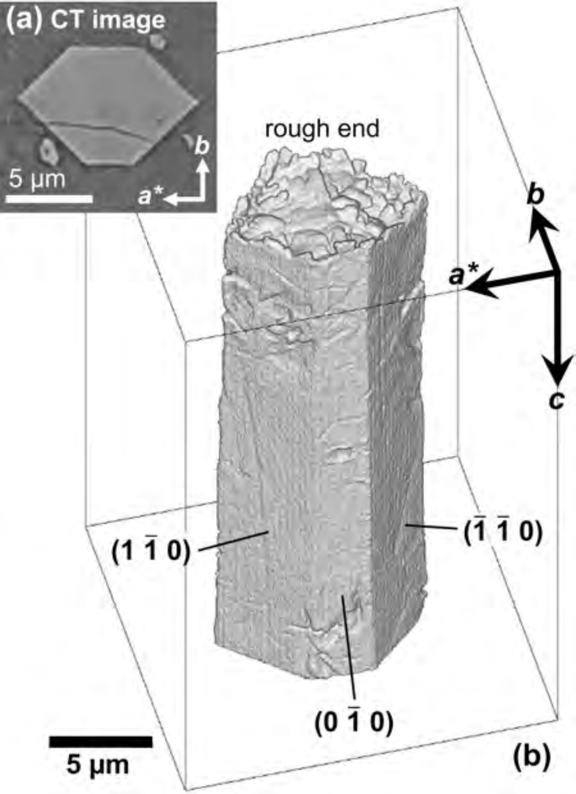

Figure 5

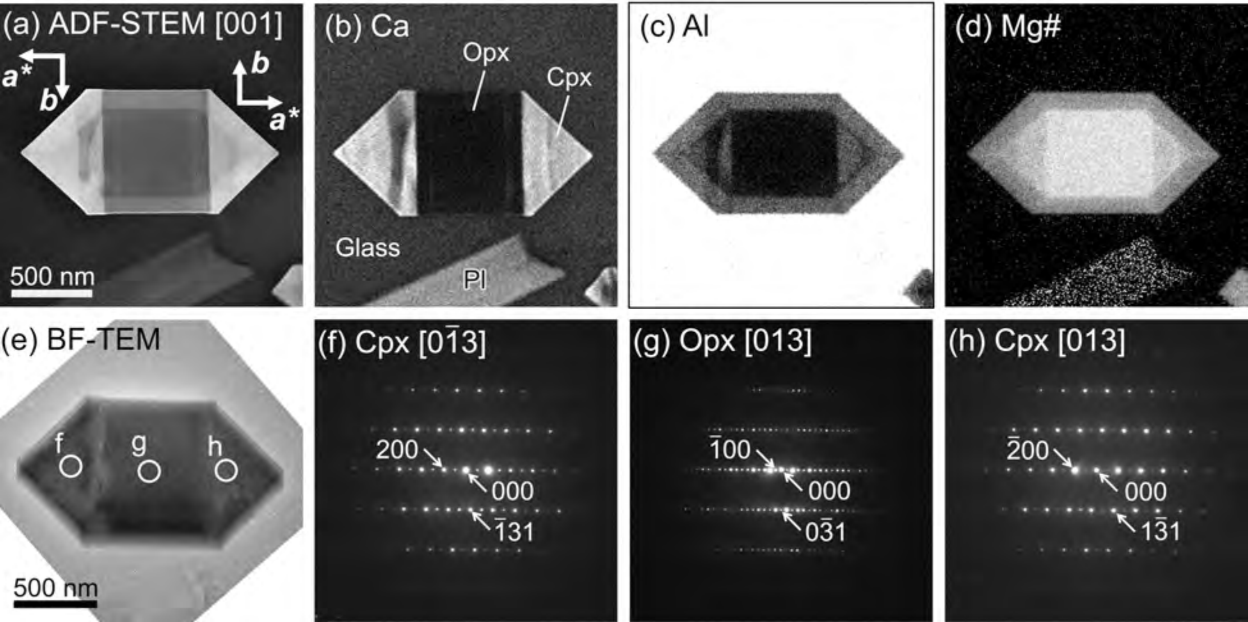
(a) ADF-STEM [001]
a*
b
b
a*
500 nm
(b) Ca
Opx
Cpx
Glass
Pl
(c) Al
(d) Mg#
(e) BF-TEM
f
g
h
500 nm
(f) Cpx [0$\bar{1}$3]
200
000
$\bar{1}$31
(g) Opx [013]
$\bar{1}$00
000
0$\bar{3}$1
(h) Cpx [013]
$\bar{2}$00
000
1$\bar{3}$1

Figure 6

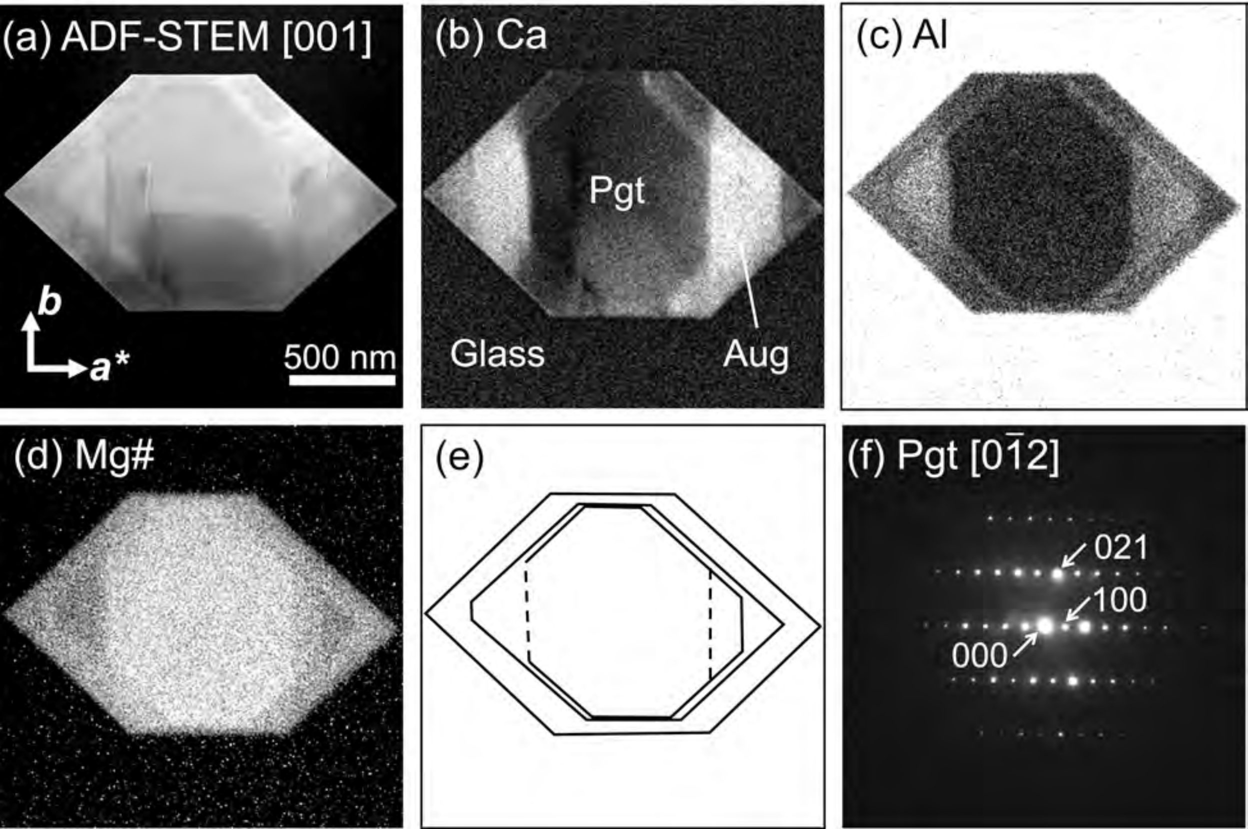
(a) ADF-STEM [001]
b
a*
500 nm
(b) Ca
Pgt
Glass
Aug
(c) Al
(d) Mg#
(e)
(f) Pgt [0$\bar{1}$2]
021
100
000

Figure 7

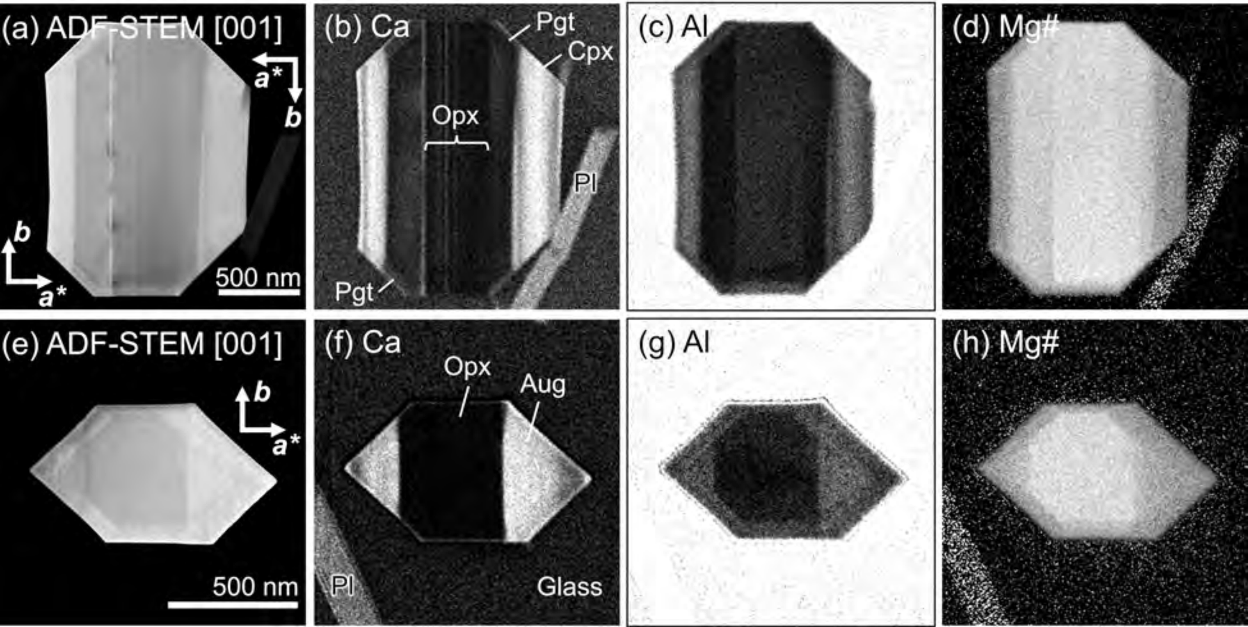
(a) ADF-STEM [001]
a*
b
b
a*
500 nm
(b) Ca
Pgt
Cpx
Opx
Pl
Pgt
(c) Al
(d) Mg#
(e) ADF-STEM [001]
b
a*
500 nm
(f) Ca
Opx
Aug
Pl
Glass
(g) Al
(h) Mg#

Figure 8

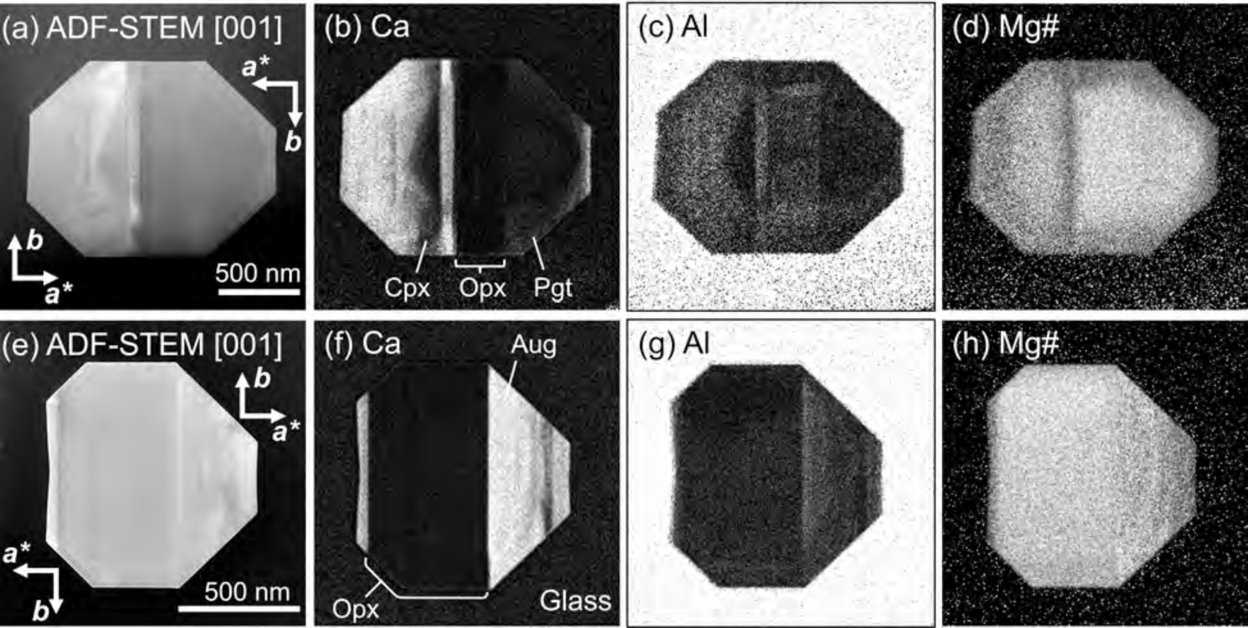
(a) ADF-STEM [001]
a*
b
b
a*
500 nm
(b) Ca
Cpx
Opx
Pgt
(c) Al
(d) Mg#
(e) ADF-STEM [001]
b
a*
a*
b
500 nm
(f) Ca
Aug
Opx
Glass
(g) Al
(h) Mg#

Figure 9

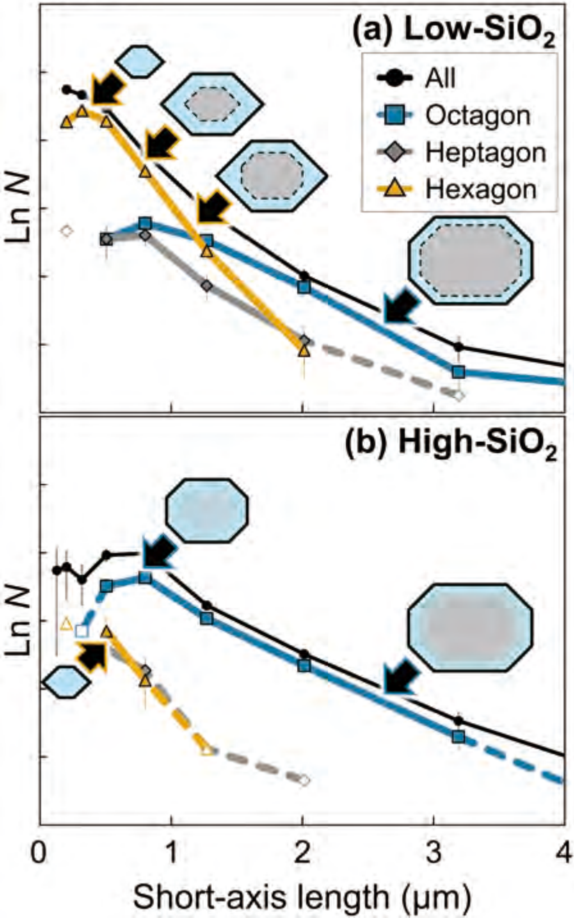
(a) Low-SiO_2
All
Octagon
Heptagon
Hexagon
Ln *N*
(b) High-SiO_2
Ln *N*
0
1
2
3
4
Short-axis length (μm)

Figure 10

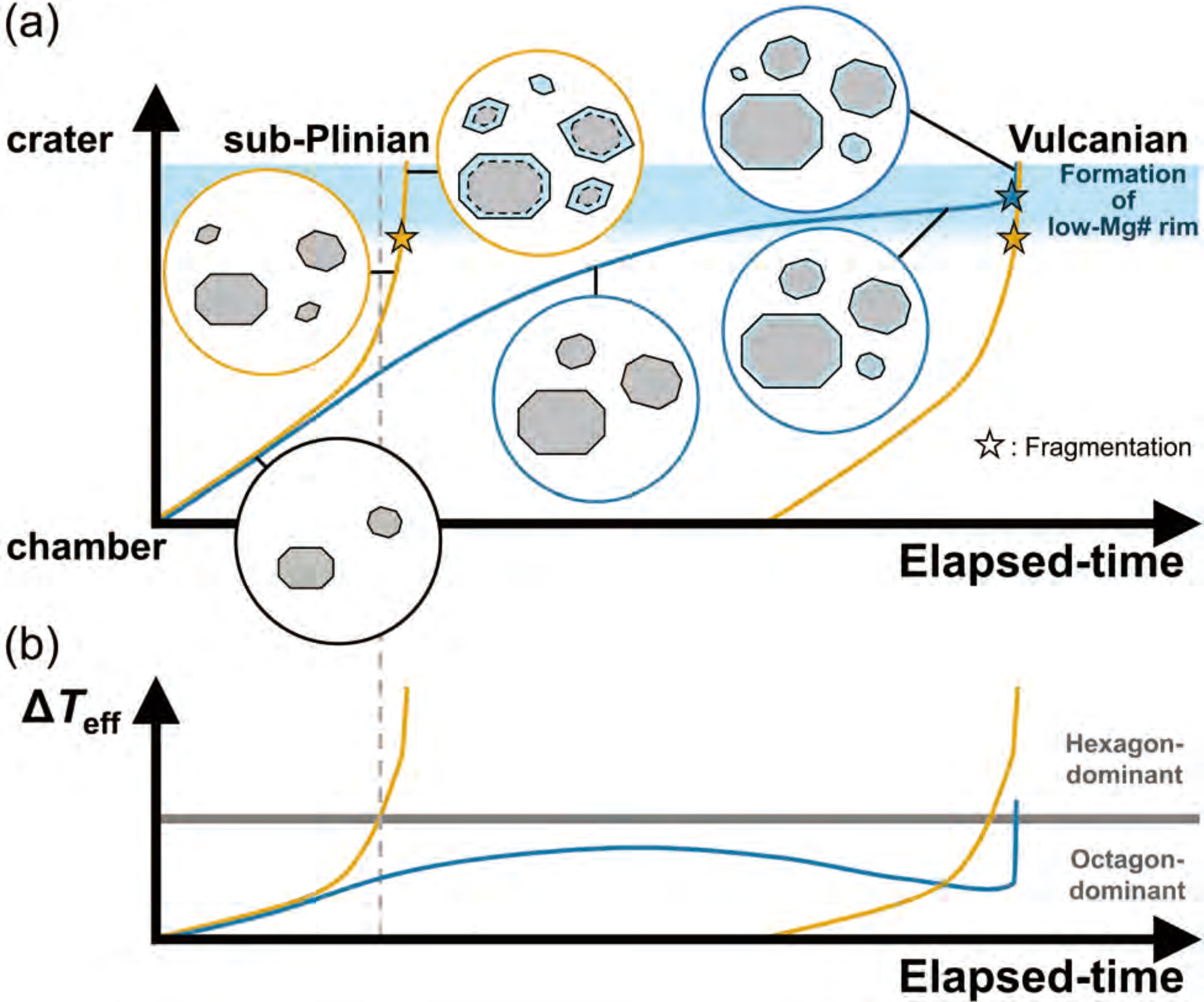
(a)
crater
sub-Plinian
Vulcanian
Formation of low-Mg# rim
☆ : Fragmentation
chamber
Elapsed-time
(b)
ΔT_{eff}
Hexagon-dominant
Octagon-dominant
Elapsed-time